JOURNAL OF GEOPHYSICAL RESEARCH, VOL. ???, XXXX, DOI:10.1002/,

Interplanetary magnetic field properties and variability near Mercury's orbit

Matthew K. James,[1] Suzanne M. Imber,[1,2] Emma J. Bunce,[1] Timothy K. Yeoman,[1]

Mike Lockwood[3,4,5] Mathew J. Owens[3,5] and James A. Slavin[6]

[1]Department of Physics and Astronomy,

This is the author manuscript accepted for publication and has undergone full peer review but has not been through the copyediting, typesetting, pagination and proofreading process, which may lead to differences between this version and the Version of Record. Please cite this article as doi: 10.1002/2017JA024435

Abstract. The first extensive study of interplanetary magnetic field (IMF) characteristics and stability at Mercury is undertaken using MESSENGER magnetometer data. Variations in IMF and solar wind conditions have a direct and rapid effect upon Mercury's highly dynamic magnetosphere; hence understanding of the time scales over which these variations occur is crucial because they

University of Leicester, Leicester LE1 7RH, UK

[2]Department of Atmospheric, Oceanic and Space Sciences, University of Michigan, Ann Arbor, Michigan, USA

[3]Department of Meteorology, University of Reading, Reading, Berkshire, RG6 6BB, UK

[4]RAL Space, Rutherford Appleton Laboratory, Chilton, Didcot, Oxfordshire, OX11 0QX, UK

[5]Space & Atmospheric Physics Group, The Blackett Laboratory, Imperial College London, London SW7 2A, UK

[6]Department of Atmospheric, Oceanic and Space Sciences, University of Michigan, Ann Arbor, Michigan, USA

determine the duration of magnetospheric states. We characterize typical distributions of IMF field strength, clock angle and cone angle throughout the duration of MESSENGER's mission. Clock and cone angle distributions collected during the first Earth year of the mission indicate that there was a significant north-south asymmetry in the location of the heliospheric current sheet during this period. The stability of IMF magnitude, clock angle, cone angle and IMF B_z polarity is quantified for the entire mission. Changes in IMF B_z polarity and magnitude are found to be less likely for higher initial field magnitudes. Stability in IMF conditions is also found to be higher at aphelion (heliocentric distance $r \sim 0.31$ AU) than at perihelion ($r \sim 0.47$ AU).

1. Introduction

The Hermean magnetosphere is often compared to that of the Earth because the dipole moments of both planets share the same sense of orientation [*Ness et al.*, 1975]. Unlike Earth, Mercury has no upstream monitor for solar wind conditions to accompany any data collected from within the Hermean magnetosphere. For planetary missions, with only a single spacecraft, the best estimate of the IMF conditions during a transit through the magnetosphere are those measured just prior to the inbound magnetopause crossing and/or just after the outbound crossing. The average properties of the IMF have been studied in the vicinity of Mercury's orbit [e.g. *Behannon*, 1978; *Burlaga*, 2001; *Korth et al.*, 2011b], though the timescales for variability of the IMF orientation and magnitude have not been characterized in great detail and studies such as that by *Korth et al.* [2011b] used only data collected during solar minimum. It is important to understand the variability of the IMF because the magnetosphere of Mercury is considerably more dynamic in comparison to that of the Earth, so at Mercury changes to the solar wind and IMF are propagated rapidly through the system and can substantially affect the magnetospheric state. The MESSENGER (MErcury Surface, Space ENvironment, GEochemistry, and Ranging) mission regularly sampled the solar wind during the time period 2011 – 2015, allowing a study of the timescales present in the IMF at Mercury during solar maximum.

While expected solar wind velocities of ~200–800 km s^{-1} at Mercury [*Russell et al.*, 1988; *Burlaga*, 2001] are similar to those experienced at 1 AU, the number density is typically up to ten times higher at ~30–70 cm^{-3} [*Burlaga*, 2001; *Blomberg et al.*, 2007; *Fujimoto et al.*, 2007]. This means that the dynamic pressure, P_{dyn}, is significantly higher at Mercury (~11.0–26.5 nPa [*Fujimoto et al.*, 2007]), which, when combined with Mercury's relatively weak dipole moment, results in a much smaller and less compressible magnetosphere at Mercury than for magnetized planets farther out from the Sun [*Glassmeier et al.*, 2004]. The magnitude of the IMF between 0.31 and 0.47 AU is typically ~20–40 nT [*Blomberg et al.*, 2007], around five times that experienced by the terrestrial magnetosphere [*Baumjohann et al.*, 2006] and daily averages measured by Helios exhibited large fluctuations which reached as much as eight times $|\mathbf{B}|$ near Earth [*Burlaga*, 2001]. The Alfvén Mach number, M_A, is lower near Mercury ($\sim$ 3.9 – 5.7) than at 1 AU ($\sim$ 9.4) [*Fujimoto et al.*, 2007] due to the larger magnitude of the IMF, and may also approach $\sim$1 during Interplanetary Coronal Mass Ejections (ICMEs), allowing the formation of Alfvén wings [*Sarantos and Slavin*, 2009].

The IMF can be considered as a spiral field as described by *Parker* [1958], purely in the R-T plane (of the RTN coordinate system, where R is the radial vector and T is in the direction of the cross product of the solar rotation axis with R), superposed with a perturbation field [*Coleman*, 1966]. Variations in the solar wind and the IMF arise partially due to higher order terms of the Sun's magnetic field [*Balogh and Smith*, 2001; *Owens and Forsyth*, 2013] and the interaction of fast and slow solar wind streams [*Russell*, 2013], and partially due to coronal holes and coronal mass ejections (CMEs). Observed variations in the IMF are largely changes in orientation rather than magnitude [e.g. *Coleman*, 1966; *Mariani and Neubauer*, 1990]. Fractional changes in IMF magnitude at Mercury are much larger than those observed at 1 AU and can be as large as the ambient IMF field strength [*Korth et al.*, 2011b].

The high intensity of the solar wind and the IMF, combined with Mercury's relatively weak intrinsic magnetic field (190 nT R_M^3, roughly 1.1% of Earth's magnetic moment [*Anderson et al.*, 2012; *Johnson et al.*, 2012]) means that Mercury has a highly active magnetosphere and undergoes extreme interaction with the solar wind and the IMF [*Siscoe and Christopher*, 1975; *Slavin*, 2004]. In addition, Mercury's magnetosphere is very small in size, with the radial distance to the subsolar magnetopause $R_{ss} \sim 1.03 - 2.0 R_M$ depending upon a combination of the dynamic pressure of the solar wind, induction effects and flux erosion of the dayside magnetosphere due to magnetic reconnection [*Siscoe and Christopher*, 1975; *Slavin and Holzer*, 1979; *Trávníček et al.*, 2007; *Slavin et al.*, 2009b; *Winslow et al.*, 2013; *Slavin et al.*, 2014; *Jia et al.*, 2015; *Zhong et al.*, 2015a, b]. A recent study by *Winslow et al.* [2017] has shown that during ∼30% of extreme interplanetary CME events, Mercury's magnetopause reaches the planetary surface.

Mercury's magnetic field has the same orientation to that of the Earth, hence it may be expected to respond to the IMF in much the same way, but due to the extreme conditions relative to Earth and lack of ionosphere to anchor field lines in place, the magnetospheric response to a change in the IMF propagates through the system much faster and is relatively more extreme [*Slavin et al.*, 2012b]. The global convection timescale at Mercury is of the order of minutes rather than hours at Earth, with a typical substorm timescale of 1-2 minutes (compared with 30–60 minutes at Earth)[*Slavin et al.*, 2009a, 2010], and a tail response time of ~1 minute (20–40 minutes at Earth) [*Siscoe and Christopher*, 1975; *Slavin and Holzer*, 1979; *Baumjohann et al.*, 2006].

The orientation of the IMF, particularly the clock angle, has a large impact on the state of the terrestrial magnetosphere. The clock angle is defined by the direction of the IMF in the Y-Z plane of the Geocentric solar-magnetospheric (GSM) coordinate system, expressed by,

$$\theta = \arctan\left(-\frac{B_y}{B_z}\right), \quad (1)$$

where $0°$ (northward) points in the +Z direction, $\pm 180°$ (southward) is in the -Z direction, $90°$ (dawnward) points towards -Y and $-90°$ (duskward) is along the Y direction. A southward IMF (negative B_z) is conducive to low latitude dayside reconnection, driving global convection of magnetic field and plasma through the magnetosphere. A B_y component of the IMF causes flux tubes to flow azimuthally, leading to asymmetries in the lobe plasma number densities [*Cowley*, 1981a; *Gosling et al.*, 1985; *Tenfjord et al.*, 2015]. The B_x component of the IMF shifts the dayside reconnection X-line southward (northward) for negative (positive) B_x [*Cowley*, 1981b] and for northward IMF can influence which polar cap undergoes lobe reconnection [*Lockwood and Moen*, 1999]. The IMF cone angle is defined as,

$$\phi = \arccos\left(-\frac{B_x}{|\mathbf{B}|}\right), \tag{2}$$

such that $\phi < 90°$ when the field has a planetward ($-B_x$) component and $\phi > 90°$ corresponds to a sunward ($+B_x$) field. The cone angle determines the location and conditions within the foreshock boundary [*Sundberg et al.*, 2013; *Le et al.*, 2013].

At Mercury, the Alfvén Mach number is of great importance to the dynamics of the magnetosphere [*Slavin and Holzer*, 1979; *Slavin et al.*, 2009a, 2012a, 2014], where the low Alfvén Mach number of the solar wind results in a low β magnetosheath and a strong plasma depletion layer (PDL) near the subsolar magnetopause [*Gershman et al.*, 2013]. Hence, the magnetic field either side of Mercury's magnetopause has a comparable magnitude and symmetric reconnection can take place more efficiently with low shear angles compared to those at Earth [*DiBraccio et al.*, 2013; *Slavin et al.*, 2014]. ICMEs which reach Mercury, such as those studied by *Winslow et al.* [2015, 2017], are likely to further reduce the Alfvén Mach number of the solar wind, particularly near Mercury's perihelion, thus increasing reconnection rates and magnetospheric convection.

Southward IMF at Earth erodes the dayside magnetosphere, reducing the subsolar distance to the magnetopause by up to 2 R_E [*Maezawa*, 1974], and causes flaring of the magnetotail as magnetic flux is transported towards the nightside [*Shue et al.*, 1997]. The same is true at Mercury, where the subsolar magnetopause reduces by 0.2–0.7 R_M and flaring increases [*Slavin and Holzer*, 1979; *Kallio and Janhunen*, 2003], although *Slavin et al.* [2014] has shown that some of the strongest reconnection effects can also be observed with northward IMF during ICMEs. The erosion of the dayside magnetopause is caused by the delay between the initiation of dayside reconnection and nightside reconnection, which at Earth is typically around 40 minutes, but at Mercury is closer to 2 minutes due to the lack of ionosphere [*Slavin and Holzer*, 1979; *Slavin et al.*, 2010] and also includes the addition of closed flux by induction in Mercury's metallic core [*Jia et al.*, 2015; *Heyner et al.*, 2016]. During southward IMF, the open flux content of Mercury's magnetosphere can increase significantly, bringing the cusps close to the equator [*Ip and Kopp*, 2002; *Kallio and Janhunen*, 2003; *Kidder et al.*, 2008; *Slavin et al.*, 2010]. Modeling of Mercury's magnetosphere has also suggested that the size and shape of the open field regions (cusps) varies both with B_x and B_z, where B_x drives a dawn-dusk asymmetry in the cusps, and negative B_z increases the size of the cusps [*Massetti et al.*, 2003; *Sarantos et al.*, 2007]. Plasma pressures in the northern cusp at Mercury, derived using magnetic pressure depressions observed by MESSENGER [*Korth et al.*, 2011a], have been shown to increase during periods of negative B_x and may also vary with B_z [*Winslow et al.*, 2012]. The increased area of the cusps during periods of negative B_z causes the magnetosphere to become flooded with sodium ions as increased solar wind particle precipitation on Mercury's surface increases the rate of sputtering [*Fujimoto et al.*, 2007; *Kidder et al.*, 2008]. Direct observations of the cusp plasma by MESSENGER have also shown increases in plasma density during large magnetic fluctuations attributed to FTE's [*Raines et al.*, 2014]. *Poh et al.* [2016] has shown that cusp filaments, a possible magnetospheric extension of FTE's, are more prevalent when solar wind conditions favor reconnection (low β and high magnetic shear angle), and may be the dominant source of energetic particle precipitation required for sputtering during extreme solar wind conditions. A more recent study by *He et al.* [2017] has shown that cusp activity is at its highest, extending over its widest range in local time, when the IMF has an antisunward and a southward component, and Mercury is nearest perihelion. *He et al.* [2017] have also shown that decreases in IMF B_y and radial distance from the Sun shift the cusp azimuthally towards dawn.

The IMF orientation and magnitude therefore play a major role in controlling Mercury's extreme dynamics. This study uses MESSENGER data to quantify the variability in the IMF orientation and magnitude with time; essential for a single spacecraft planetary mission such as MESSENGER. These short timescales for responses in Mercury's magnetosphere and the lack of an upstream monitor make it critically important to understand how the IMF is likely to have varied once the observing craft has moved inside the magnetosphere, so that probabilities can be placed on interpretations of the inferred causes of changes and structures seen inside the magnetosphere.

2. Data

The data used to perform this study were collected using the MESSENGER Magnetometer (MAG) which sampled the magnetic field near Mercury at up to 20 Hz [*Anderson et al.*, 2007] from 23 March 2011 to 30 April 2015. Due to the highly inclined and elliptical nature of both MESSENGER's initial 12 hour and final 8 hour orbits, MESSENGER sampled the magnetosheath and the IMF upstream of the bow shock.

It was necessary to separate the IMF data taken in the solar wind from that collected in the magnetosheath or the magnetosphere. *Winslow et al.* [2013] used changes in magnetic field characteristics, such as changes in magnitude, orientation and variability to determine bow shock (BS) and magnetopause (MP) boundary crossings between 23 March 2011 and 19 December 2011. Due to the high variability in the location of both boundaries, there are often multiple crossings of the same boundary during a single pass. *Winslow et al.* [2013] defined each group of these crossings as a single boundary crossing. We have employed the same method to locate the remaining boundary crossings until the end of the mission. The IMF data used is that which lies between the outermost BS crossing on the outbound section of MESSENGER's orbit, and the outermost BS crossing on the inbound section of the orbit. Due to the complexity of the solar wind interaction with Mercury's magnetic field during intervals of extreme solar wind conditions (see *Slavin et al.* [2014]) we have excluded CME's intervals from our study. The CME events which were excluded from our study were characterized by large distortions of the Hermean magnetic field and an imperceptible difference between solar wind and magnetosheath data, possibly due to low solar wind Alfvén Mach numbers. The magnetosheath data is also collected between the innermost BS crossing and outermost MP crossing on each orbit.

In order to remove any high frequency variability and biasing in data distributions due to changes in sample rate, the data were initially reduced to a 10 second average. For the timescale aspect of this study, the data was also smoothed using a 1 minute sliding window (which needs to be compared to the typical Dungey cycle duration of ~2 minutes at Mercury [*Slavin et al.*, 2010]) to reduce the presence of upstream waves in the data. This leaves longer period variations which are likely to cause longer-lasting changes to the state of the Hermean magnetosphere.

The data products are supplied in the Mercury solar-magnetospheric (MSM) reference frame, where x is the line from the center of the Hermean dipole to the Sun, y points towards dusk and z is directed along the Hermean dipole axis. The Hermean dipole is approximately in line with the rotational axis, but is displaced by $\sim 0.196 R_M$ into the northern hemisphere of the planet

[*Anderson et al.*, 2012; *Johnson et al.*, 2012]. For the purpose of this investigation, these values were used to determine a field magnitude, $|\mathbf{B}|$, clock angle, θ, and cone angle, ϕ.

The observed Parker spiral angle (PSA) at Mercury can also be determined using

$$\alpha = \arctan\left(-\frac{B_y}{B_x}\right). \tag{3}$$

In order to determine the maximum amount that each IMF parameter p (i.e. magnitude, clock angle or cone angle) is likely to change with time t, an algorithm looped through each value p_i at time t_i, determining the maximum deviation from this value (Δp) within m different time ranges ΔT_j. This resulted in m different time series of maximum deviations in p for each ΔT_j, where values of ΔT_j used were in the range of 1 minute – 4 hours (a range covering all the residence times of MESSENGER in Mercury's magnetosphere). The maximum deviations for each ΔT_j are then placed in n bins of size Δp_k, forming a 2D histogram of size $m \times n$. Each of the m columns of this histogram is then normalized, providing a probability that somewhere within the time range t_i to $t_i + \Delta T_j$, the parameter p will have departed from its original value by Δp_{k-1} to Δp_k. We here adopt values of ΔT in 21 evenly spaced logarithmic steps from 60 s to 14400 s which capture the important features on the required timescales.

The probability of a flip in IMF B_z polarity is also here investigated in a similar manner to the other parameters. For each data point, in each time range bin, the result will be 1 if a reversal has occurred and 0 if there has not been a flip in polarity. As this is simply a binary result rather than a range, there is no need to place the result into range bins. Instead, a probability for a B_z polarity reversal within a time range bin is calculated by dividing the sum of all the 1s by the total number of 0s and 1s within those bins. This study therefore provides a comparison with the assessment of IMF stability performed at Mercury by *He et al.* [2017] and the corresponding study for near-Earth interplanetary space by [*Lockwood et al.*, 2016].

3. Results

3.1. IMF Distributions

Figure 1 a, b and c show the distributions of magnetic field magnitude, clock angle and cone angle, respectively for the IMF, where panels d, e and f show the equivalent distributions for the magnetosheath. The modal IMF strength in Figure 1a is ~20 nT, where ~71 % of the measurements were within the range of 10 – 30 nT and relatively few (< 1 %) measurements are made above 60 nT. The corresponding distribution in magnetosheath field strength has a much larger spread in values, with a peak around 34 nT, almost doubling the IMF field strength (this being an average for the parts of the sheath sampled by MESSENGER).

Figure 1b depicts a bimodal distribution of clock angles, with peaks at 90 and -90°, where there is some level of bias toward a clock angle of 90° present in this distribution. Similarly, the cone angles in Figure 1c show a bimodal distribution, with peaks near 35 and 150°, where there is also a bias toward the latter peak.

The clock angle distribution measured within the Hermean magnetosheath in Figure 1e has a similar bimodal nature to the IMF clock angle distribution, with some slight bias toward dawnward-oriented clock angles. This distribution is very similar to the IMF clock angle distribution with an anti-clockwise rotation of ~20°.

The cone angle distribution for the magnetosheath in Figure 1f shows a similar bimodal distribution to that in Figure 1c, where there is a bias toward sunward oriented cone angles. The primary difference here is a general shift in the distribution towards 90° cone angles, as peaks are close to 45 and 135°.

Figures 2 and 3 show the magnetic field magnitude ($|\mathbf{B}|$), clock angle and cone angle distributions created using a subset of the data used in Figure 1 taken within 5 % of Mercury's orbital major axis of perihelion (0.307 – 0.315 AU) and aphelion (0.459 – 0.467 AU). The magnetic field strengths observed near perihelion are significantly higher than those near aphelion, with modal values of ~30 and 15 nT, respectively. The bimodality of the clock angle distribution is less pronounced at perihelion, while rotation of the magnetosheath clock angle distribution appears to be much more significant. The bias in cone angle distribution at perihelion is in the opposite direction to that observed at aphelion and in Figure 1. Mercury spends much longer near to aphelion than perihelion due to the eccentricity of Mercury's orbit, such that Figure 3 is made up of a somewhat larger amount of data than Figure 2, though both subsets of data are still large (1.35×10^6 IMF vectors at Aphelion and 1.02×10^6 IMF vectors at Perihelion).

The variation in Parker Spiral Angle (PSA) at Mercury with distance from the Sun is presented in Figure 4, where the PSAs calculated using Equation 3 have been split into 50 orbital distance bins and 180 angular bins. The distributions in each of the 50 distance bins have been normalized between 0 and 1 such that they share the same color scale, where the distribution peaks appear in yellow. The solid black line shows the modal value of Gaussians fitted to each distribution. This line fits well with the expected PSA, shown as a dotted line, given an assumed solar wind speed of 400 km s^{-1} [*Coleman*, 1966].

3.2. IMF Parameter Variation Timescales

The short term variations in the IMF magnitude are presented in Figure 5 (a – c), using the parameter ΔB. ΔB is the maximum absolute change in the magnetic field strength in a given time range ΔT. Each panel is formatted such that the time range, ΔT, lies along the x-axis, ΔB is on the y-axis and probability is in color. The color scale for these plots is logarithmic, due to the relatively low probabilities calculated for the majority of the bins. Figure 5a is the probability calculated using data from all parts of Mercury's orbit around the sun, while figures 5b and 5c show the probabilities calculated using only data near perihelion and aphelion, respectively. The top row in each grid represents all changes in field magnitude where $\Delta B > 58$ nT. The probabilities are independently calculated for each time bin, where the probabilities in each column all sum to equal 1, and represent the probability that there is a change in $|\mathbf{B}|$ at any time between the initial field measurement and the corresponding ΔT following the measurement. Figure 5d is in a similar format to that of panels a – c, but instead shows the variability of the parameter $\Delta B/|\mathbf{B}|$, where the maximum change in magnetic field magnitude has been scaled by the initial measured magnitude for reasons which are discussed below.

In all panels of Figure 5, the probability that there is very little change in the IMF magnitude is highest for the shortest time ranges. As the time range from the initial measurement increases, larger changes in field magnitude become the most probable, while the probability distributions spread over a larger range in ΔB. When comparing the perihelion (panel b) and aphelion (panel c), the IMF magnitude appears to be somewhat more stable near aphelion. There is a significant reduction in magnetic field magnitude from perihelion to aphelion, as seen in Figures 2a and 3a, so a proportional reduction in ΔB from perihelion to aphelion should be expected. When ΔB is scaled by the initial measurement of magnetic field magnitude to become $\Delta B/|\mathbf{B}|$, the difference between perihelion and aphelion disappears, such that the probabilities presented in Figure 5d can be used for any part of the Hermean orbit around the Sun.

Figure 6 shows the probability of clock angle change with time, where panel a is using all of the data collected, b is for near perihelion and c is for near aphelion. Each plot is a polar plot, where the radial axis represents the time range since measurement, the azimuthal axis shows the amount by which clock angle has changed in degrees. The probability of that change is given by the color, using the same logarithmic color scale used in Figure 5. The dotted line in each panel shows the location of the peak in the probability distributions with time.

All plots in Figure 6 look very similar, with a high probability of very little change in clock angle after just a short time ($P(|\Delta\theta| < 20°) = 37\%$ within 5 minutes of measurement), but the probability distributions spread out for longer times. A closer inspection shows that the probability of a change in clock angle is slightly higher at perihelion than at aphelion; within 5 minutes of the initial measurement, the probability that the maximum deviation in clock angle is less than 20° is $P(|\Delta\theta| < 20°|R < 0.315\text{AU}) = 32\%$ and $P(|\Delta\theta| < 20°|R > 0.459\text{AU}) = 41\%$ for perihelion and aphelion, respectively, where R is the orbital radius of Mercury.

The probability of cone angle change with time is presented in Figure 7 using a similar to format to Figure 6, just with a maximum change in cone angle of 180°. In these plots, the probability of a change in cone angle follows the same pattern as with clock angle and ΔB, where distributions spread out with time and favor larger changes in cone angle at larger time ranges. Overall the probability that the maximum deviation of clock angle is less than $10°$ for 5 minutes since the last measurement is $P(|\Delta\phi| < 10°) = 37\%$. The equivalent probabilities measured using data collected near aphelion and perihelion are $P(|\Delta\phi| < 10°|R < 0.315\text{AU}) = 34\%$ and $P(|\Delta\phi| < 10°|R > 0.459\text{AU}) = 40\%$, respectively, showing that there is an increase in the stability of the cone angle with radial distance from the Sun, as was observed with the clock angle.

Figure 8 shows the probability of a sign change in B_z with time after a measurement for a) all IMF data, b) data collected close to perihelion and c) data collected near to aphelion. Each line represents a 5 nT bin in initial IMF magnitude between 0 and 60 nT, where the darker lines represent higher field strength bins. The grayed-out lines in each plot are those where not enough data existed at high initial field strengths to form the probability distribution correctly.

In all panels of Figure 8, for all initial field magnitudes, the probability of a sign change in B_z starts off relatively low, and tends towards 1 with time. The rate at which this probability increases is strongly related to initial field strength - smaller initial field magnitudes are more likely to see a sign change in B_z sooner than higher ones. The probability of a change in B_z polarity is also generally higher near perihelion than near aphelion. *Lockwood et al.* [2016] (their figure 14) show that in near-Earth interplanetary space, the overall probability of a B_z polarity change after 4 hours is 0.83, which is lower than the average in all panels of figure 8 for such a lag. Hence the difference between perihelion and aphelion found here is a trend that continues with increasing heliocentric distance to $r = 1$AU. *He et al.* [2017] assessed the stability of each component of the IMF at Mercury over a 40 minute time period, using a 15 minute average of each component and found that B_z was the least stable of the three components, where there was a correlation of ~ 0.64 with the estimated value for B_z and the measured B_z at ± 40 minutes time difference. The analysis undertaken by this study shows that, after 40 minutes since the last measurement of the IMF, there is a 70% chance of the sign of B_z remaining the same for large initial field magnitudes, but only $\sim 13\%$ chance of B_z keeping its polarity for small initial field values.

4. Discussion

4.1. Clock Angle Rotation in the Magnetosheath

In Figures 1, 2 and 3, the transition from solar wind to magnetosheath field has an associated rotation in the clock angle distributions. At aphelion, this rotation was less obvious then at perihelion, where the distribution of clock angles had rotated significantly.

Figure 9 uses 10 minute averages of IMF and magnetosheath data to investigate the rotation of the clock angles. To simplify the investigation, only bow shock crossings with a Parker spiral-like orientation of the IMF were used, where positive (negative) B_x was accompanied by negative (positive) B_y. Panels a), b) and c) show the clock angle distributions for the 10 minutes of data collected just outside of each bow shock crossing, just inside each bow shock crossing and just outside of the magnetopause, respectively. Panels d) and e) show distributions of changes in clock angle, where d is the change in clock angle from the solar wind to just inside the bow shock and e is the change in clock angle from the solar wind to just outside of the magnetopause. The blue line in both of these plots represents a Gaussian function of the form $f(\Delta\theta) = A\mathrm{e}^{\frac{-(\Delta\theta-\mu)^2}{2\sigma^2}}$ fitted to the distribution, which is used to calculate the expected rotation, μ. The final panel, (f), shows the distributions of change in clock angle across the bow shock against radial distance from the Sun, where the red line with circular markers shows the peak in each distribution.

The largest difference in clock angle between the unshocked solar wind and magnetosheath occurs closest to the bow shock boundary, the difference is much smaller when comparing the IMF to the magnetosheath field close to the magnetopause. This suggests that the transition through the shock may be mostly responsible for the rotation, rather than the continued draping caused by the magnetosheath flow of field lines around the magnetosphere, which may actually be rotating the field lines back towards their pre-shocked orientation. The rotation of an individual magnetic field vector due to a shock is to be expected if the vector has a component tangential to the shock. According to the Rankine-Hugoniot relations, the normal component of $\mathbf{B}$ is conserved but, due to the step in velocity across the shock, the tangential component of this vector must change in order to compensate and conserve the electric field [*Kivelson and Russell*, 1995]. The angle by which the field rotates will be dependent upon the initial orientation of the IMF and the location on the bow shock where the rotation is measured.

The rotation of individual field vectors across the bow shock is explained above, but the rotation of an entire distribution of these vectors is explained schematically using Figure 10. Panel a shows the direction of both sunward and antisunward field lines forming an Archimedian spiral as described by *Parker* [1958], where the frame of reference is observing the northern hemisphere of the Sun as it rotates anticlockwise. The red, sunward field lines have a positive B_x and a negative B_y, and the green antisunward field lines have a negative B_x and positive B_y component in the MSM coordinate system. Panel b shows Mercury in the Mercury Solar Magnetic (MSM) coordinate system (centered upon the dipole of Mercury, 0.19 R_M north of Mercury's equatorial plane [*Anderson et al.*, 2011, 2012; *Johnson et al.*, 2012]) where the Sun is to the left and the observer is facing the dusk side of the planet. The blue and cyan lines show the model magnetopause and bow shock boundaries, respectively, while the red and orange ellipses represent the extreme orbital configurations of MESSENGER in this plane.

In both the 12 hour (orange) and 8 hour (red) orbital configurations, MESSENGER mostly sampled the solar wind and magnetosheath south of the planetary magnetic equator. Due to the small Parker spiral angle at Mercury (Figure 4), we assume that the IMF is mostly radial in Figure 10b, where the red and the green field lines sunward of the bow shock correspond to sunward and planetward directed field lines above and below the heliospheric current sheet, respectively (panel a). The red and green field lines planetward of the bow shock represent shocked/draped magnetic field lines and have gained a component in the positive or negative B_z direction. For both sunward and antisunward field lines, the shock generates an anticlockwise rotation across the boundary for field lines below the planetary magnetic equator because the

B_z becomes more positive (negative) while -(+)B_y remains constant. A rotation in the opposite sense would have occurred if MESSENGER's orbit had been reversed in z, and mostly sample northern bow shock crossings.

The significant difference in rotation of the clock angle distributions at perihelion and aphelion (Figures 2 and 3, respectively) could suggest that this effect is larger closer to the Sun, though Figure 9f shows that there is little obvious change in the rotation with radial distance from the Sun. Hence, a more likely explanation for the increased rotation at perihelion would be that MESSENGER samples the flanks of a relatively smaller bow shock at perihelion than at aphelion, where the normal of the bow shock at the crossings near aphelion are more oblique to the solar wind flow, thus a smaller rotation of $\mathbf{B}$ occurs at aphelion than at perihelion.

4.2. Long-Term Temporal Variations and Asymmetries in IMF Distributions

In Figures 1, 2 and 3 there are some significant asymmetries in the clock and cone angle distributions. For Figures 1 and 3, there are more measurements of clock angles in the range $0 < \theta < 180°$ and cone angles $\phi > 90°$, corresponding to sunward-oriented field lines. In Figure 2, the asymmetry is reversed, with slightly more measurements of clock angles in the range $-180 < \theta < 0°$ and cone angles in the range $\phi < 90°$, corresponding to antisunward IMF. This suggests that Mercury spent more time on one side of the heliospheric current sheet (HCS) for a significant time during the MESSENGER mission.

The orbit of Mercury is inclined by ~3.4° to the Sun's equator, with an argument of perihelion of ~29° meaning that perihelion lies north of the solar equator and aphelion is south of the solar equator. If the HCS was perfectly symmetric about the solar equatorial plane, then there would be a bias towards the observation of one IMF polarity at aphelion and the other at perihelion.

This bias should be evident when the clock angle and cone angle distributions are split up by radial distance from the Sun, but no such trend was observed overall.

Figure 11 shows the variations in the parameter distributions for the IMF (panels a - c) and magnetosheath (panels d to f) throughout the MESSENGER mission, where panels a) and d) are the magnetic field magnitude, b) and e) are the clock angle and c) and f) are the cone angle distributions. Each distribution is taken over an 88 Earth day period (one Mercury year) in order to remove any effects due to the eccentric orbit of Mercury, and is normalized between 0 and 1, where red represents a peak in the distribution. It is obvious from this plot that the IMF orientation distributions are highly variable over long periods of time and that effects observed in the IMF are propagated into the magnetosheath. Vertical dashed lines present in each panel define three periods of different activity.

It appears that the overall shift in the distributions observed in Figure 1 originated mostly within the first 5 Mercury years of MESSENGER's mission (period 1), where antisunward IMF observations were relatively infrequent compared to those which were sunward. The sunward bias is presented in panel b as a large, dominant peak in clock angles ~90 ° combined with a dominant peak in cone angles $> 90°$ in panel c. Period 2 contains more variability in the IMF orientation distributions and, while sunward IMF observations are still prevalent, the numbers of sunward and antisunward IMF measurements are slightly more evenly matched. Finally, the IMF measurements made during period 3 were more of the opposite sense to period 1, where the IMF was generally antisunward.

MESSENGER orbited Mercury near to the sunspot maximum of solar cycle 24, during which the Sun underwent an atypical reversal in magnetic polarity, where the northern and southern hemispheres reversed in polarity at different times [*Sun et al.*, 2015; *Lockwood et al.*, 2017].

Lockwood et al. [2017] discussed this reversal in polarity in great detail by splitting the solar maximum into 5 distinct time periods, and using the hemispherically asymmetrical emergence of bipolar magnetic regions (BMRs) to explain the asymmetrical reversal.

The first of these time periods corresponds approximately to period 1 of Figure 11, where the northern hemisphere experienced a peak in sunspot numbers and underwent a reversal in magnetic polarity. *Lockwood et al.* [2017] suggested that BMR emergence in the northern hemisphere reconnected with the northern polar field, generating more open solar flux (OSF) and sunward-oriented field lines close to the solar equator during this time. Distributions in the IMF B_x component from MESSENGER near Mercury and Omni2 near Earth during this time period were shown to agree with this theory, where the sunward IMF polarity was dominant in both datasets.

During the second time period of *Lockwood et al.* [2017], approximately in line with period 2 of Figure 11, the sunspot numbers in both hemispheres were similar. The northern field had already reversed, but the southern hemisphere was yet to flip. During this time symmetric BMR emergence was proposed to be driving the polar flux transport suggesting that equal amounts of sunward and antisunward field should have been present at both Mercury and Earth. MESSENGER and Omni2 data showed that there were almost equal amounts of both IMF polarities measured during this time.

The third and fourth time periods from *Lockwood et al.* [2017] correspond to the remainder of the MESSENGER mission, period 3 of Figure 11. It is during this time that the southern hemisphere reversed in magnetic polarity and had a peak in sunspot numbers. In this case *Lockwood et al.* [2017] suggested that asymmetric BMR emergence in the southern hemisphere allowed it to catch up with the northern hemisphere. This led to antisunward flux at the solar equator, which was visible in the MESSENGER and Omni2 datasets from this time period. The final time period in *Lockwood et al.* [2017] is beyond the lifetime of the MESSENGER mission.

4.3. Implications for Magnetospheric Dynamics

Both short-term and long-term changes in the IMF can influence the dynamics of the Hermean magnetosphere. The IMF conditions directly affect magnetospheric phenomena such as global convection dynamics, magnetotail structure and dynamics, plasma populations and particle precipitation. Variations in the IMF on timescales similar to magnetospheric processes can more readily force the magnetosphere [*Korth et al.*, 2011b], driving large, substorm-like events *Slavin et al.* [2012b].

The long-term variations in the IMF parameter distributions are visible in Figure 11, where there are significant changes in both magnitude and orientation of the IMF which would have driven long-term modulations of Hermean magnetospheric dynamics. During the long period of predominantly sunward-oriented IMF in the first ~5 Hermean years after MESSENGER's orbital insertion (period 1 of Figure 11), the magnetosphere would have experienced a prolonged period of positive B_x and negative B_y. At Earth, positive B_x moves the northern polar cap tailward and the southern polar cap sunward [*Cowley*, 1981b], while negative B_y would drive the azimuthal flow of reconnected flux tubes and increase the plasma densities in the northern, dusk-side and the southern dawn-side tail lobes [*Gosling et al.*, 1985]. If Mercury's magnetosphere responded to the IMF orientation in the same way as Earth, then it could have a similar, but more enhanced reaction to this IMF configuration, with increased cusp plasma pressure [*Winslow et al.*, 2012] and enhanced plasma flows in the north [*Varela et al.*, 2015]. The reversal of the predominant IMF direction near the end of the MESSENGER mission would also have had a similar effect on the magnetosphere but in the opposite hemisphere.

At Earth the reconnection rate is highly dependent upon the shear angle between the IMF and the terrestrial field. The dayside reconnection rate can be expressed as

$$\Phi = B_{\perp} V_s L, \tag{4}$$

where $B_{\perp}$ is the magnitude of the IMF in the $Y - Z$ GSM plane, V_{sw} is the solar wind speed. L is a function of the IMF clock angle θ, where one functional form of L is that used by *Perreault and Akasofu* [1978], where $L = L_0 \sin^4\left(\frac{\theta}{2}\right)$, which is zero for purely northward IMF ($\theta = 0$) and gradually increases to L_0 for purely southward IMF.

The above half-wave recifier model for reconnection at Earth is less applicable at Mercury due to the low Alfvénic Mach number resulting in a low β in the magnetosheath [*Gershman et al.*, 2013]. *DiBraccio et al.* [2013] suggested that the reconnection rate, Φ, at Mercury was independent of IMF orientation, but inversely proportional to the plasma β parameter. β is the ratio of the plasma pressure to the magnetic pressure and can be expressed as:

$$\beta = \frac{2nk_B T \mu_0}{B^2}, \tag{5}$$

where n is the plasma number density, k_B is the Boltzmann constant, T is the plasma temperature, μ_0 is the permeability of free space and B is the magnetic field strength. The IMF magnitude in Figure 11 is typically around 20 nT throughout the mission, apart from the penultimate Hermean year, where the modal field magnitude almost doubles to ~35 nT. If $\Phi \propto \frac{1}{\beta}$, then $\Phi \propto B^2$, such that the increase in IMF magnitude near the end of the mission could potentially have tripled the reconnection rate.

Figures 5, 6 and 7 show how the IMF magnitude and orientation varies on shorter time scales (< 4 hours) and Figure 8 shows the likelihood of a change in the IMF north-south polarity with time. Previous studies have suggested that the variation in the IMF is mostly in orientation rather than magnitude *Coleman* [e.g. 1966]; *Jackman* [e.g. 2004], but Figure 5 shows that there are still some noticeable and important variations in $|\mathbf{B}|$ on relatively short time scales. The field magnitude is still likely to be within 10% of its original value in the first 20 minutes after measurement and within 20% after ~30 – 60 minutes (depending upon initial field magnitude). This implies that convection rates for the first 30–60 minutes since the last IMF measurement are likely to remain relatively stable providing that the clock and cone angles have not changed.

The IMF $|\mathbf{B}|$ and clock angle variations can also be compared to the earlier work of *Korth et al.* [2011b], where cruise phase data collected by MESSENGER was used to provide a similar analysis of the IMF conditions close to Mercury's orbit. *Korth et al.* [2011b] determined the probability that the IMF magnitude would remain within some maximum deviation, δB_{max}, for 2 and 4 hours at a time, where four different values of δB_{max} were used (1, 2, 5 and 10 nT). Table 1 shows the probabilities for each δB_{max} calculated using the data from this study in black, compared to the values obtained by *Korth et al.* [2011b] in red. In all cases, the probability that IMF $|\mathbf{B}|$ remained within δB_{max} was found to be somewhat lower for this study.

Korth et al. [2011b] also calculated the probability that the clock angle would change by less than $\delta\theta_{max}$ within 2 and 4 hours, where six values were used for $\delta\theta_{max}$ (10, 30, 60, 90, 120 and 150°). Table 2 shows the probabilities calculated in this study in black and those provided by *Korth et al.* [2011b] in red. Much like the field magnitude, the probability that clock angle changes by less than $\delta\theta_{max}$ is considerably less in this study than that calculated by *Korth et al.* [2011b], for all values of $\delta\theta_{max}$.

A possible explanation for the higher variability in $|\mathbf{B}|$ and clock angle in this study, compared that found by *Korth et al.* [2011b], is related to the two different time periods from which the datasets originated. The data in this study was collected between 2011 and 2015 which corresponds to solar maximum. The data collected during the cruise phase of MESSENGER was collected from 2007 to 2011 which was during the solar minimum. The *Korth et al.* [2011b] study also focused on data collected in the region of Mercury's orbit from 0.31 – 0.47 AU. *Korth et al.* [2011b] made the suggestion that the IMF may be more active during the time that MESSENGER was in orbit of Mercury as solar activity would be higher. The implication of this is that the timescales on which the Hermean magnetosphere could potentially change configuration are markedly shorter near solar maximum.

The overall timescale on which the IMF is likely to change in magnitude or orientation significantly is of the order of a few tens of minutes. This is larger than the typical convection timescale of the Hermean magnetosphere. A consequence of this is that the solar wind conditions are unlikely to remain stable for more than 10–20 minutes and that any measurements of the IMF prior to entering the magnetosheath are only likely to be applicable to measurements taken in the magnetosphere within this time range. *He et al.* [2017] uses IMF measurements taken $\sim$ 40 minutes before or after transiting the cusp, which our results suggest that the clock and cone angles may deviate by as much as $\sim 90°$ and $\sim 40°$, respectively. There is also likely to be a change in $\Delta B/|\mathbf{B}|$ by up to 15% within 40 minutes. Due to the rapid reaction time of the magnetosphere to changes in the IMF, there is little delay time for a global magnetospheric response to a change in the IMF. The crossing through the magnetosheath can be significantly longer than the variability timescale of the IMF so a measure of the magnetosheath field may be more relevant than that of the IMF, although care must be take as the relative orientations of the field in the magnetosheath and the IMF are dependent upon location.

5. Conclusion

In this study we used MESSENGER magnetometer data to characterize the typical properties of the IMF and timescales for changes in field magnitude and orientation between 0.31 and 0.47 AU. There is a marked difference in IMF properties between aphelion and perihelion, particularly the field magnitude.

The IMF distributions have been shown to vary significantly in predominant orientation on long-term timescales, where the first 5 Hermean years of the MESSENGER mission at Mercury saw a predominantly sunward-oriented IMF and the last few Hermean years the opposite orientation was dominant. These changes in predominant field orientation are due to the reversal in the solar magnetic field occurring at different times in both hemispheres. Long-term variations in the typical field magnitude were also observed, where the IMF was significantly stronger near to the end of the MESSENGER mission.

The short term variations in the IMF were found to occur on slightly longer timescales than the magnetospheric convection timescale, though not by much. The exact time scales were found to be dependent upon radial distance from the Sun, where the IMF appeared to be slightly more stable at aphelion than at perihelion. It is estimated that the IMF is likely to retain a similar state for 10 – 20 minutes, but over longer periods of time there are likely to be significant differences in the IMF, driving different magnetospheric states. These timescales are also compared to results from a study of the IMF in the region of Mercury's orbit during solar minimum [*Korth et al.*, 2011b], and it is found that the variation timescales obtained by this study at solar maximum are noticeably shorter than those at solar minimum.

The typical characteristics of the IMF and how it varies with time, as determined from this study, could influence efforts to model the interaction of the Hermean magnetosphere with the solar wind. The data here provide essential context for future analysis of the MESSENGER data from within the magnetosphere. The statistics provided here are also likely to be applicable during the arrival of BepiColombo in 2025 during the next solar maximum. *Yoshida and Yamagishi* [2010] proposed that there is a correlation between the IMF magnitude and the monthly average sun spot number, where higher sun spot numbers corresponded to higher field magnitudes. The recent solar maximum of cycle 24 was unusually weak, if sun spot numbers during cycle 25 are more typical of previous solar cycles, then BepiColombo may routinely observe higher field magnitudes than those observed in this study.

Acknowledgments. The work by M.K.J., S.M.I, T.K.Y. and E.J.B. is supported by STFC grant ST/H002480/1. S.M.I. is also supported by the Leverhulme Trust. The work of M.L. and M.J.O. is supported by STFC grant ST/M000885/1. One of the authors (J.A.S.) was supported by NASA's Heliophysics Supporting Research (NNX15AJ68G) and Living With a Star (NNX16AJ67G) programs. The MESSENGER project is supported by the NASA Discovery Program under contracts NASW-00002 to the Carnegie Institution of Washington and NAS5-97271 to The Johns Hopkins Applied Physics Laboratory. The data used in this study are available from the Planetary Data Center.

References

Anderson, B. J., M. H. Acuña, D. A. Lohr, J. Scheifele, A. Raval, H. Korth, and J. A. Slavin, The Magnetometer Instrument on MESSENGER, *Space Sci. Rev.*, *131*(1-4), 417–450, doi:10.1007/s11214-007-9246-7, 2007.

Anderson, B. J., C. L. Johnson, H. Korth, M. E. Purucker, R. M. Winslow, J. a. Slavin, S. C. Solomon, R. L. McNutt, J. M. Raines, and T. H. Zurbuchen, The Global Magnetic Field of

Mercury from MESSENGER Orbital Observations, *Science (80-.).*, *333*(6051), 1859–1862, doi:10.1126/science.1211001, 2011.

Anderson, B. J., C. L. Johnson, H. Korth, R. M. Winslow, J. E. Borovsky, M. E. Purucker, J. A. Slavin, S. C. Solomon, M. T. Zuber, and R. L. McNutt, Low-degree structure in Mercury's planetary magnetic field, *J. Geophys. Res.-Planet.*, *117*(E12), doi:10.1029/2012JE004159, e00L12, 2012.

Balogh, A., and E. J. Smith, The heliospheric magnetic field at solar maximum: Ulysses observations, *Space Science Reviews*, *97*(1), 147–160, doi:10.1023/A:1011854901760, 2001.

Baumjohann, W., A. Matsuoka, K. Glassmeier, C. Russell, T. Nagai, M. Hoshino, T. Nakagawa, A. Balogh, J. Slavin, R. Nakamura, and W. Magnes, The magnetosphere of Mercury and its solar wind environment: Open issues and scientific questions, *Adv. Sp. Res.*, *38*(4), 604–609, doi:10.1016/j.asr.2005.05.117, 2006.

Behannon, K. W., Heliocentric distance dependence of the interplanetary magnetic field, *Rev. Geophys.*, *16*(1), 125, doi:10.1029/RG016i001p00125, 1978.

Blomberg, L. G., J. A. Cumnock, K.-H. Glassmeier, and R. A. Treumann, Plasma Waves in the Hermean Magnetosphere, *Space Sci. Rev.*, *132*(2-4), 575–591, doi:10.1007/s11214-007-9282-3, 2007.

Burlaga, L., Magnetic fields and plasmas in the inner heliosphere: Helios results, *Planetary and Space Science*, *49*(14), 1619 – 1627, doi:http://dx.doi.org/10.1016/S0032-0633(01)00098-8, 2001.

Coleman, P. J., Variations in the interplanetary magnetic field: Mariner 2: 1. observed properties, *Journal of Geophysical Research*, *71*(23), 5509–5531, doi:10.1029/JZ071i023p05509, 1966.

Cowley, S., Magnetospheric asymmetries associated with the y-component of the IMF, *Planetary and Space Science*, *29*(1), 79 – 96, doi:http://dx.doi.org/10.1016/0032-0633(81)90141-0, 1981a.

Cowley, S., Asymmetry effects associated with the x-component of the IMF in a magnetically open magnetosphere, *Planetary and Space Science*, *29*(8), 809 – 818, doi: http://dx.doi.org/10.1016/0032-0633(81)90071-4, 1981b.

DiBraccio, G. A., J. A. Slavin, S. A. Boardsen, B. J. Anderson, H. Korth, T. H. Zurbuchen, J. M. Raines, D. N. Baker, R. L. McNutt, and S. C. Solomon, MESSENGER observations of magnetopause structure and dynamics at Mercury, *Journal of Geophysical Research: Space Physics*, *118*(3), 997–1008, doi:10.1002/jgra.50123, 2013.

Fujimoto, M., W. Baumjohann, K. Kabin, R. Nakamura, J. A. Slavin, N. Terada, and L. Zelenyi, Hermean Magnetosphere-Solar Wind Interaction, *Space Sci. Rev.*, *132*(2-4), 529–550, doi: 10.1007/s11214-007-9245-8, 2007.

Gershman, D. J., J. A. Slavin, J. M. Raines, T. H. Zurbuchen, B. J. Anderson, H. Korth, D. N. Baker, and S. C. Solomon, Magnetic flux pileup and plasma depletion in Mercury's subsolar magnetosheath, *J. Geophys. Res. Sp. Phys.*, *118*(11), 7181–7199, doi: 10.1002/2013JA019244, 2013.

Glassmeier, K.-H., D. Klimushkin, C. Othmer, and P. Mager, ULF waves at Mercury: Earth, the giants, and their little brother compared, *Adv. Sp. Res.*, *33*(11), 1875–1883, doi: 10.1016/j.asr.2003.04.047, 2004.

Gosling, J. T., D. N. Baker, S. J. Bame, W. C. Feldman, R. D. Zwickl, and E. J. Smith, North-south and dawn-dusk plasma asymmetries in the distant tail lobes: ISEE 3, *J. Geophys. Res.*, *90*(A7), 6354, doi:10.1029/JA090iA07p06354, 1985.

He, M., J. Vogt, D. Heyner, and J. Zhong, Solar wind controls on Mercury's magnetospheric cusp, *Journal of Geophysical Research: Space Physics*, *122*(6), 6150–6164, doi:10.1002/2016JA023687, 2016JA023687, 2017.

Heyner, D., C. Nabert, E. Liebert, and K.-H. Glassmeier, Concerning reconnection-induction balance at the magnetopause of Mercury, *Journal of Geophysical Research: Space Physics*, *121*(4), 2935–2961, doi:10.1002/2015JA021484, 2015JA021484, 2016.

Ip, W.-H., and A. Kopp, MHD simulations of the solar wind interaction with Mercury, *Journal of Geophysical Research: Space Physics*, *107*(A11), SSH 4–1–SSH 4–8, doi:10.1029/2001JA009171, 1348, 2002.

Jackman, C. M., Interplanetary magnetic field at ~9 AU during the declining phase of the solar cycle and its implications for Saturn's magnetospheric dynamics, *J. Geophys. Res.*, *109*(A11), A11,203, doi:10.1029/2004JA010614, 2004.

Jia, X., J. A. Slavin, T. I. Gombosi, L. K. S. Daldorff, G. Toth, and B. van der Holst, Global MHD simulations of Mercury's magnetosphere with coupled planetary interior: Induction effect of the planetary conducting core on the global interaction, *Journal of Geophysical Research: Space Physics*, *120*(6), 4763–4775, doi:10.1002/2015JA021143, 2015JA021143, 2015.

Johnson, C. L., M. E. Purucker, H. Korth, B. J. Anderson, R. M. Winslow, M. M. H. Al Asad, J. A. Slavin, I. I. Alexeev, R. J. Phillips, M. T. Zuber, and S. C. Solomon, MESSENGER observations of Mercury's magnetic field structure, *J. Geophys. Res.-Planet.*, *117*(E12), doi:10.1029/2012JE004217, 2012.

Kallio, E., and P. Janhunen, Solar wind and magnetospheric ion impact on Mercury's surface, *Geophys. Res. Lett.*, *30*(17), n/a–n/a, doi:10.1029/2003GL017842, 1877, 2003.

Kidder, A., R. M. Winglee, and E. M. Harnett, Erosion of the dayside magnetosphere at Mercury in association with ion outflows and flux rope generation, *J. Geophys. Res. -Space*, *113*(A9), n/a–n/a, doi:10.1029/2008JA013038, a09223, 2008.

Kivelson, M. G., and C. T. Russell, *Introduction to Space Physics*, Cambridge University Press, 1995.

Korth, H., B. J. Anderson, J. M. Raines, J. A. Slavin, T. H. Zurbuchen, C. L. Johnson, M. E. Purucker, R. M. Winslow, S. C. Solomon, and R. L. McNutt, Plasma pressure in Mercury's equatorial magnetosphere derived from MESSENGER Magnetometer observations, *Geophys. Res. Lett.*, *38*(22), n/a–n/a, doi:10.1029/2011GL049451, 2011a.

Korth, H., B. J. Anderson, T. H. Zurbuchen, J. A. Slavin, S. Perri, S. A. Boardsen, D. N. Baker, S. C. Solomon, and R. L. McNutt, The interplanetary magnetic field environment at Mercury's orbit, *Planet. Space Sci.*, *59*(15), 2075–2085, doi:10.1016/j.pss.2010.10.014, 2011b.

Le, G., P. J. Chi, X. Blanco-Cano, S. Boardsen, J. A. Slavin, B. J. Anderson, and H. Korth, Upstream ultra-low frequency waves in Mercury's foreshock region: MESSENGER magnetic field observations, *J. Geophys. Res. Sp. Phys.*, *118*(6), 2809–2823, doi:10.1002/jgra.50342, 2013.

Lockwood, M., and J. Moen, Reconfiguration and closure of lobe flux by reconnection during northward IMF: possible evidence for signatures in cusp/cleft auroral emissions, *Annales Geophysicae*, *17*(8), 996–1011, doi:10.1007/s00585-999-0996-2, 1999.

Lockwood, M., M. J. Owens, L. A. Barnard, S. Bentley, C. J. Scott, and C. E. Watt, On the origins and timescales of geoeffective IMF, *Space Weather*, *14*(6), 406–432, doi:10.1002/2016SW001375, 2016SW001375, 2016.

Lockwood, M., M. J. Owens, S. M. Imber, M. K. James, E. J. Bunce, and T. K. Yeoman, Coronal and heliospheric magnetic flux circulation and its relation to open solar flux evolution, *J. Geophys. Res.*, doi:10.1002/2016JA023644, 2017.

Maezawa, K., Dependence of the magnetopause position on the southward interplanetary magnetic field, *Planet. Space Sci.*, *22*(10), 1443–1453, doi:10.1016/0032-0633(74)90040-3, 1974.

Mariani, F., and F. M. Neubauer, *The Interplanetary Magnetic Field*, p. 183, Springer Science & Business Media, 2012, 1990.

Massetti, S., S. Orsini, A. Milillo, A. Mura, E. D. Angelis, H. Lammer, and P. Wurz, Mapping of the cusp plasma precipitation on the surface of Mercury , *Icarus*, *166*(2), 229 – 237, doi: https://doi.org/10.1016/j.icarus.2003.08.005, 2003.

Ness, N. F., K. W. Behannon, R. P. Lepping, and Y. C. Whang, The magnetic field of Mercury, 1, *Journal of Geophysical Research*, *80*(19), 2708–2716, doi:10.1029/JA080i019p02708, 1975.

Owens, M. J., and R. J. Forsyth, The heliospheric magnetic field, *Liv Rev. So. Phys.*, *10*(1), 5, doi:10.12942/lrsp-2013-5, 2013.

Parker, E. N., Dynamics of the Interplanetary Gas and Magnetic Fields., *Astrophys. J.*, *128*, 664, doi:10.1086/146579, 1958.

Perreault, P., and S.-I. Akasofu, A study of geomagnetic storms, *Geophysical Journal of the Royal Astronomical Society*, *54*(3), 547–573, doi:10.1111/j.1365-246X.1978.tb05494.x, 1978.

Poh, G., J. A. Slavin, X. Jia, G. A. DiBraccio, J. M. Raines, S. M. Imber, D. J. Gershman, W.-J. Sun, B. J. Anderson, H. Korth, T. H. Zurbuchen, R. L. McNutt, and S. C. Solomon, MESSENGER observations of cusp plasma filaments at Mercury, *Journal of Geophysical*

Research: Space Physics, *121*(9), 8260–8285, doi:10.1002/2016JA022552, 2016JA022552, 2016.

Raines, J. M., D. J. Gershman, J. A. Slavin, T. H. Zurbuchen, H. Korth, B. J. Anderson, and S. C. Solomon, Structure and dynamics of Mercury's magnetospheric cusp: MESSENGER measurements of protons and planetary ions, *Journal of Geophysical Research: Space Physics*, *119*(8), 6587–6602, doi:10.1002/2014JA020120, 2014JA020120, 2014.

Russell, C. T., Solar Wind and Interplanetary Magnetic Field: A Tutorial, in *Sp. Weather Geophys. Monogr. Ser. Vol. 125*, vol. 125, pp. 73–89, Wiley-AGU, doi:10.1029/GM125p0073, 2013.

Russell, C. T., D. N. Baker, and J. A. Slavin, The Magnetosphere of Mercury, in *Mercury*, edited by F. Vilas, C. R. Chapman, and M. S. Matthews, pp. 514 – 561, Univ. of Ariz. Press, Tucson, Ariz., 1988.

Sarantos, M., and J. A. Slavin, On the possible formation of Alfvén wings at Mercury during encounters with coronal mass ejections, *Geophysical Research Letters*, *36*(4), n/a–n/a, doi:10.1029/2008GL036747, l04107, 2009.

Sarantos, M., R. M. Killen, and D. Kim, Predicting the long-term solar wind ion-sputtering source at mercury, *Planetary and Space Science*, *55*(11), 1584 – 1595, doi:https://doi.org/10.1016/j.pss.2006.10.011, Relation between Exosphere-Magnetosphere-Surface on Mercury and the Moon European Geosciences Union , 2007.

Shue, J.-H., J. K. Chao, H. C. Fu, C. T. Russell, P. Song, K. K. Khurana, and H. J. Singer, A new functional form to study the solar wind control of the magnetopause size and shape, *J. Geophys. Res. Sp. Phys.*, *102*(A5), 9497–9511, doi:10.1029/97JA00196, 1997.

Siscoe, G., and L. Christopher, Variations in the solar wind stand-off distance at Mercury, *Geophys. Res. Lett.*, *2*(4), 158–160, doi:10.1029/GL002i004p00158, 1975.

Slavin, J., Mercury's magnetosphere, *Adv. Sp. Res.*, *33*(11), 1859–1874, doi: 10.1016/j.asr.2003.02.019, 2004.

Slavin, J. A., and R. E. Holzer, The effect of erosion on the solar wind stand-off distance at Mercury, *Journal of Geophysical Research: Space Physics*, *84*(A5), 2076–2082, doi: 10.1029/JA084iA05p02076, 1979.

Slavin, J. A., M. H. Acuña, B. J. Anderson, D. N. Baker, M. Benna, S. A. Boardsen, G. Gloeckler, R. E. Gold, G. C. Ho, H. Korth, S. M. Krimigis, R. L. McNutt, J. M. Raines, M. Sarantos, D. Schriver, S. C. Solomon, P. Trávníček, and T. H. Zurbuchen, MESSENGER Observations of Magnetic Reconnection in Mercury's Magnetosphere, *Science*, *324*(5927), 606–610, doi:10.1126/science.1172011, 2009a.

Slavin, J. A., B. J. Anderson, T. H. Zurbuchen, D. N. Baker, S. M. Krimigis, M. H. Acuña, M. Benna, S. A. Boardsen, G. Gloeckler, R. E. Gold, G. C. Ho, H. Korth, R. L. McNutt, J. M. Raines, M. Sarantos, D. Schriver, S. C. Solomon, and P. Trávníček, MESSENGER observations of Mercury's magnetosphere during northward IMF, *Geophys. Res. Lett.*, *36*(2), doi:10.1029/2008GL036158, 2009b.

Slavin, J. A., B. J. Anderson, D. N. Baker, M. Benna, S. A. Boardsen, G. Gloeckler, R. E. Gold, G. C. Ho, H. Korth, S. M. Krimigis, R. L. McNutt, L. R. Nittler, J. M. Raines, M. Sarantos, D. Schriver, S. C. Solomon, R. D. Starr, P. M. Travnicek, and T. H. Zurbuchen, MESSENGER Observations of Extreme Loading and Unloading of Mercury's Magnetic Tail, *Science*, *329*(5992), 665–668, doi:10.1126/science.1188067, 2010.

Slavin, J. A., B. J. Anderson, D. N. Baker, M. Benna, S. A. Boardsen, R. E. Gold, G. C. Ho, S. M. Imber, H. Korth, S. M. Krimigis, R. L. McNutt, J. M. Raines, M. Sarantos, D. Schriver, S. C. Solomon, P. Trávníček, and T. H. Zurbuchen, MESSENGER and Mariner 10 flyby observations of magnetotail structure and dynamics at Mercury, *J. Geophys. Res. Sp. Phys.*, *117*(A1), doi:10.1029/2011JA016900, 2012a.

Slavin, J. A., S. M. Imber, S. A. Boardsen, G. A. DiBraccio, T. Sundberg, M. Sarantos, T. Nieves-Chinchilla, A. Szabo, B. J. Anderson, H. Korth, T. H. Zurbuchen, J. M. Raines, C. L. Johnson, R. M. Winslow, R. M. Killen, R. L. McNutt, and S. C. Solomon, MESSENGER observations of a flux-transfer-event shower at Mercury, *J. Geophys. Res. Sp. Phys.*, *117*(A12), doi:10.1029/2012JA017926, 2012b.

Slavin, J. A., G. A. DiBraccio, D. J. Gershman, S. M. Imber, G. K. Poh, J. M. Raines, T. H. Zurbuchen, X. Jia, D. N. Baker, K.-H. Glassmeier, S. A. Livi, S. A. Boardsen, T. A. Cassidy, M. Sarantos, T. Sundberg, A. Masters, C. L. Johnson, R. M. Winslow, B. J. Anderson, H. Korth, R. L. McNutt, and S. C. Solomon, MESSENGER observations of Mercury's dayside magnetosphere under extreme solar wind conditions, *J. Geophys. Res. Sp. Phys.*, *119*(10), 8087–8116, doi:10.1002/2014JA020319, 2014.

Sun, X., J. T. Hoeksema, Y. Liu, and J. Zhao, On polar magnetic field reversal and surface flux transport during solar cycle 24, *The Astrophysical Journal*, *798*(2), 114, 2015.

Sundberg, T., S. A. Boardsen, J. A. Slavin, V. M. Uritsky, B. J. Anderson, H. Korth, D. J. Gershman, J. M. Raines, T. H. Zurbuchen, and S. C. Solomon, Cyclic reformation of a quasi-parallel bow shock at Mercury: MESSENGER observations, *J. Geophys. Res. Sp. Phys.*, *118*(10), 6457–6464, doi:10.1002/jgra.50602, 2013.

Tenfjord, P., N. Ø stgaard, K. Snekvik, K. M. Laundal, J. P. Reistad, S. Haaland, and S. E. Milan, How the IMF By induces a By component in the closed magnetosphere and how it leads to asymmetric currents and convection patterns in the two hemispheres, *Journal of Geophysical Research: Space Physics*, *120*(11), 9368–9384, doi:10.1002/2015JA021579, 2015JA021579, 2015.

Trávníček, P., P. Hellinger, and D. Schriver, Structure of Mercury's magnetosphere for different pressure of the solar wind: Three dimensional hybrid simulations, *Geophys. Res. Lett.*, *34*(5), 1–5, doi:10.1029/2006GL028518, 2007.

Varela, J., F. Pantellini, and M. Moncuquet, The effect of interplanetary magnetic field orientation on the solar wind flux impacting Mercury's surface, *Planet. Space Sci.*, *119*, 264–269, doi:10.1016/j.pss.2015.10.004, 2015.

Winslow, R. M., C. L. Johnson, B. J. Anderson, H. Korth, J. A. Slavin, M. E. Purucker, and S. C. Solomon, Observations of Mercury's northern cusp region with MESSENGER's Magnetometer, *Geophys. Res. Lett.*, *39*(8), doi:10.1029/2012GL051472, 2012.

Winslow, R. M., B. J. Anderson, C. L. Johnson, J. A. Slavin, H. Korth, M. E. Purucker, D. N. Baker, and S. C. Solomon, Mercury's magnetopause and bow shock from MESSENGER Magnetometer observations, *J. Geophys. Res. Sp. Phys.*, *118*(5), 2213–2227, doi:10.1002/jgra.50237, 2013.

Winslow, R. M., N. Lugaz, L. C. Philpott, N. A. Schwadron, C. J. Farrugia, B. J. Anderson, and C. W. Smith, Interplanetary coronal mass ejections from MESSENGER orbital observations at Mercury, *Journal of Geophysical Research: Space Physics*, *120*(8), 6101–6118, doi:10.1002/2015JA021200, 2015JA021200, 2015.

Winslow, R. M., L. Philpott, C. S. Paty, N. Lugaz, N. A. Schwadron, C. L. Johnson, and H. Korth, Statistical study of ICME effects on Mercury's magnetospheric boundaries and northern cusp region from MESSENGER, *Journal of Geophysical Research: Space Physics*, *122*(5), 4960–4975, doi:10.1002/2016JA023548, 2016JA023548, 2017.

Yoshida, A., and H. Yamagishi, Predicting amplitude of solar cycle 24 based on a new precursor method, *Annales Geophysicae*, *28*(2), 417–425, doi:10.5194/angeo-28-417-2010, 2010.

Zhong, J., W. X. Wan, J. A. Slavin, Y. Wei, R. L. Lin, L. H. Chai, J. M. Raines, Z. J. Rong, and X. H. Han, Mercury's three-dimensional asymmetric magnetopause, *Journal of Geophysical Research: Space Physics*, *120*(9), 7658–7671, doi:10.1002/2015JA021425, 2015JA021425, 2015a.

Zhong, J., W. X. Wan, Y. Wei, J. A. Slavin, J. M. Raines, Z. J. Rong, L. H. Chai, and X. H. Han, Compressibility of Mercury's dayside magnetosphere, *Geophysical Research Letters*, *42*(23), 10,135–10,139, doi:10.1002/2015GL067063, 2015GL067063, 2015b.

δB_{max}	Probability (%) within:	
	2 hours	4 hours
$\leq$ 1 nT	< 0.1 (2.9)	< 0.1 (0.3)
$\leq$ 2 nT	1.3 (8.9)	0.2 (2.6)
$\leq$ 5 nT	22.4 (33.0)	8.8 (15.7)
$\leq$ 10 nT	67.6 (74.1)	47.9 (55.1)

Table 1. Probabilities calculated for $|\mathbf{B}|$ to vary by less than δB_{max} within 2 and 4 hours of measurement. Values in (red) are those obtained by *Korth et al.* [2011b] for comparison.

$\delta\theta_{max}$	Probability (%) within:	
	2 hours	4 hours
$\leq$ 10°	< 0.1 (0.4)	< 0.1 (0.0)
$\leq$ 30°	1.8 (5.0)	0.4 (1.7)
$\leq$ 60°	9.8 (17.3)	3.0 (8.3)
$\leq$ 90°	20.7 (32.8)	8.7 (16.7)
$\leq$ 120°	32.9 (46.3)	17.0 (26.9)
$\leq$ 150°	44.3 (60.9)	26.1 (39.3)

Table 2. Probabilities calculated for clock angle, θ, to vary by less than $\delta\theta_{max}$ within 2 and 4 hours of measurement. Values in (red) are those obtained by *Korth et al.* [2011b] for comparison.

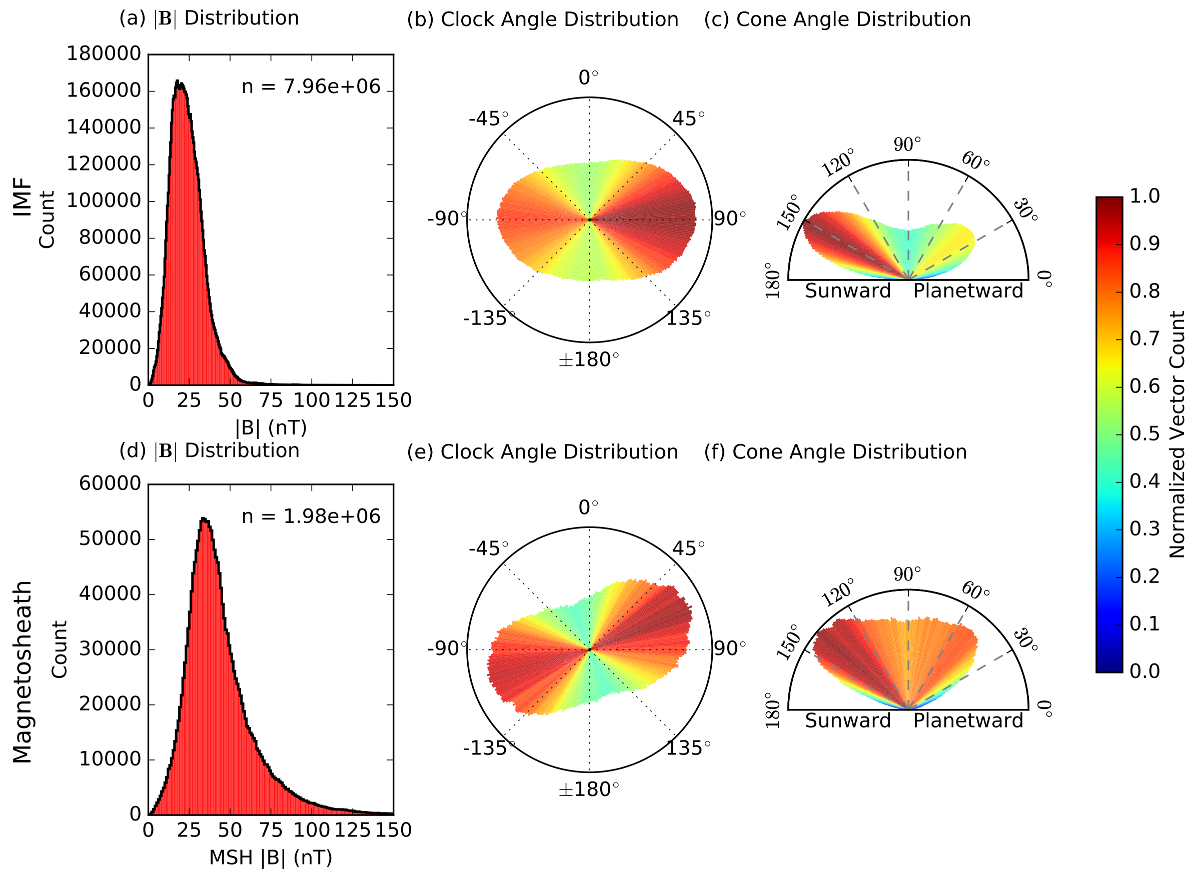

Figure 1. Distributions of interplanetary magnetic field (a-c) and magnetosheath (d-f) data collected during the primary and extended stages of the MESSENGER mission. Panels a and d show the distributions of the magnetic field magnitude. Panels b and e show the clock angles as measured by MESSENGER, where the radial axis represents the occurrence of each clock angle. A clock angle of 0° represents a northward field and 90° represents a dawnward oriented field. Panels c and f show the distribution of cone angles detected by MESSENGER where the radial axis represents the count and the rotational axis represents the cone angle. A cone angle of 0° is defined here as a purely planetward oriented field, while a cone angle of 180° is purely sunward. The color of the bars in the clock and cone angle distributions is related to the bar length, where a higher count results in a red color and a lower count is represented by blue.

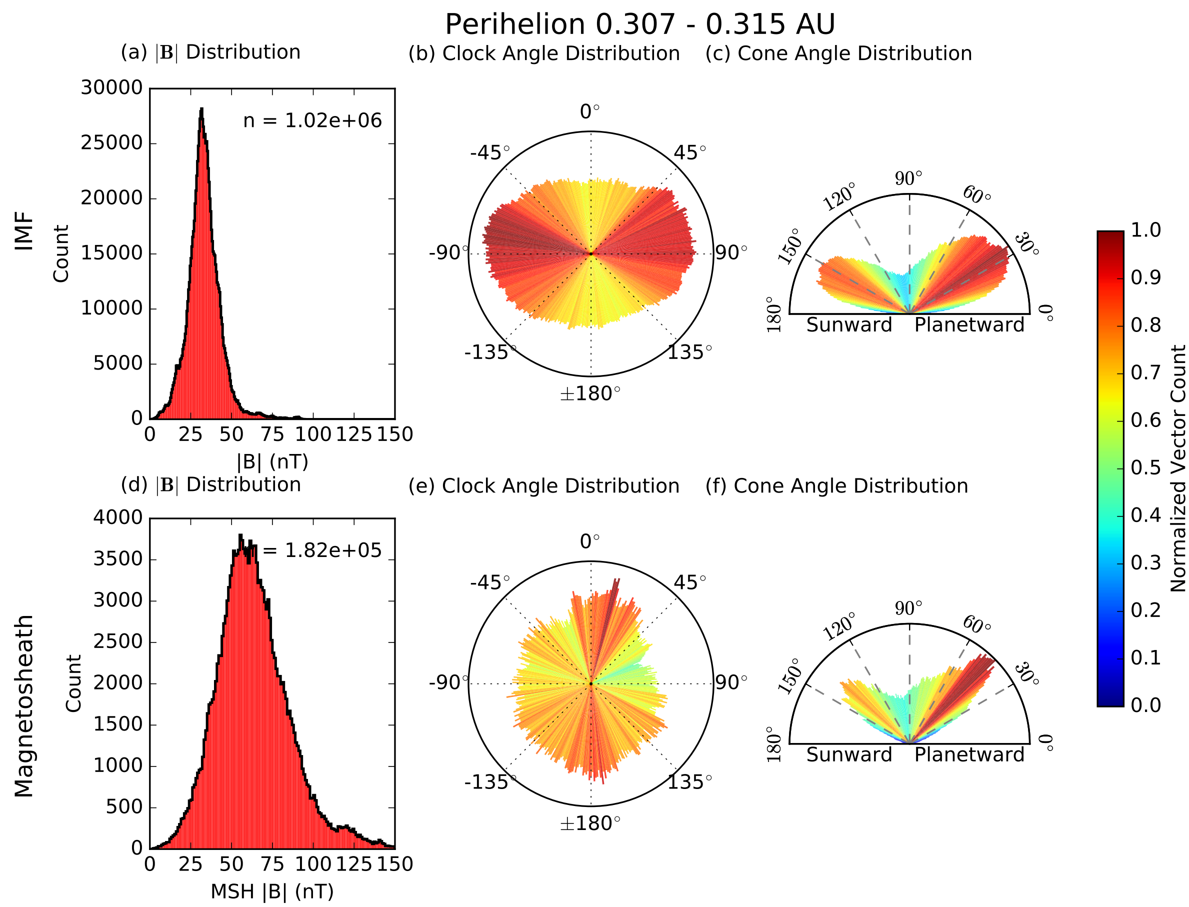

Figure 2. Distributions of the interplanetary magnetic field and the magnetosheath collected near perihelion, using the same format as Figure 1.

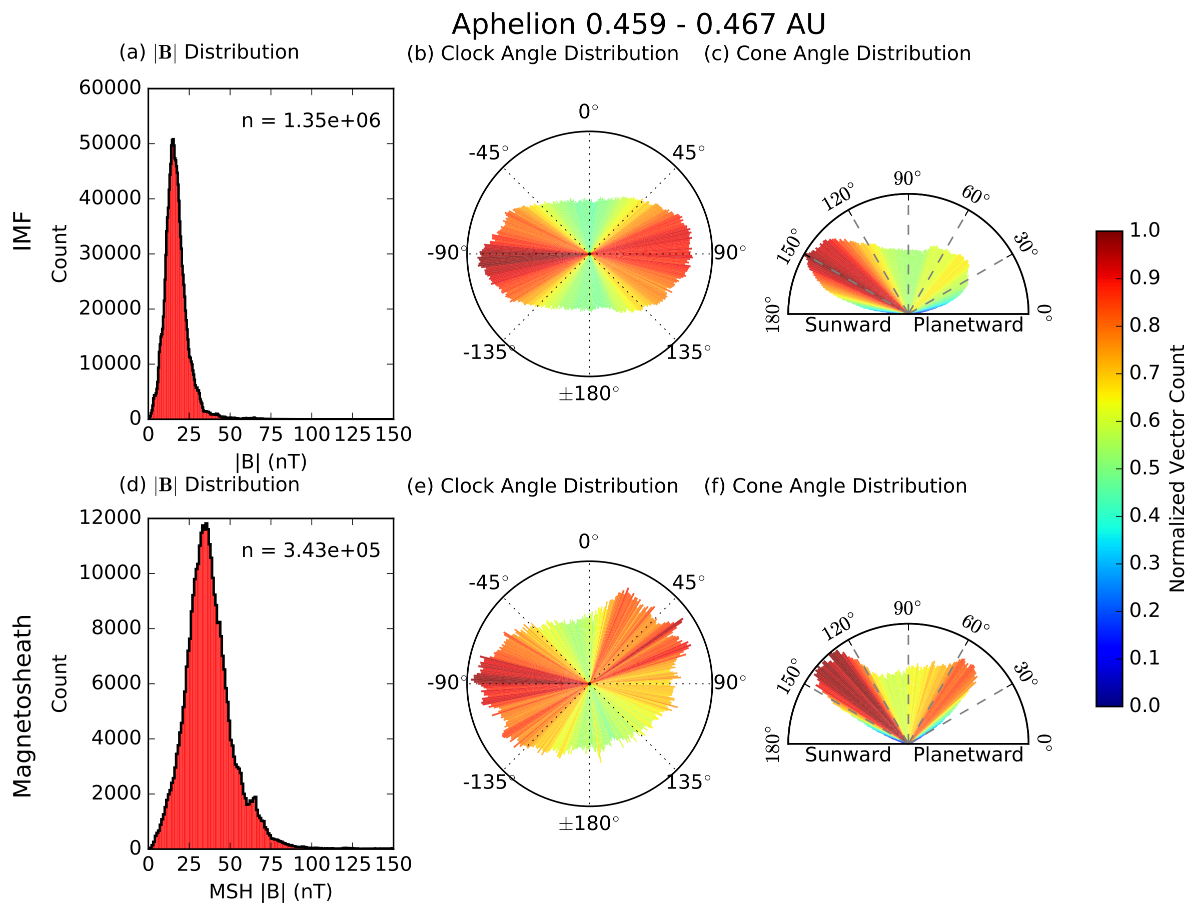

Figure 3. Distributions of the interplanetary magnetic field and the magnetosheath collected near aphelion, using the same format as Figure 1.

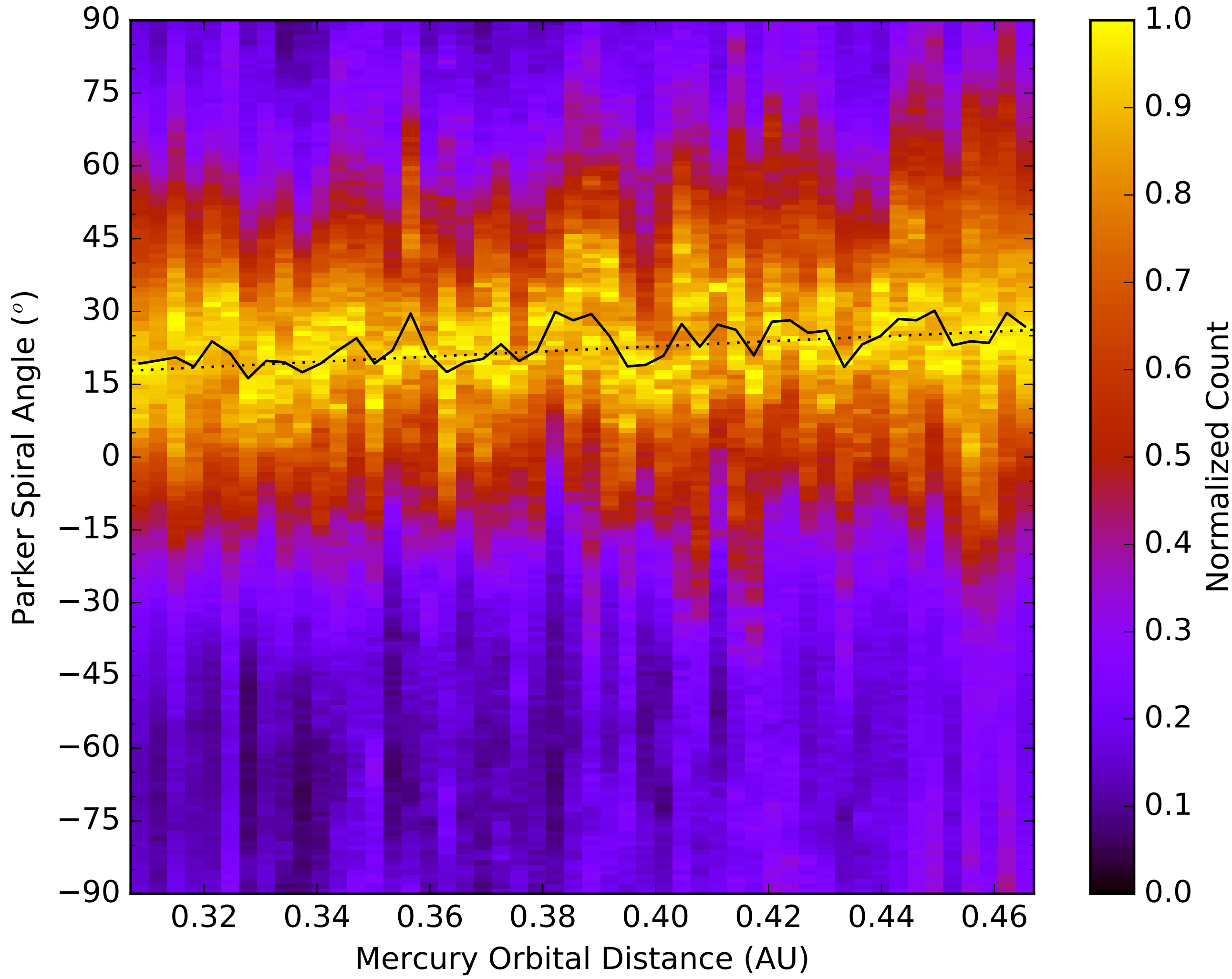

Figure 4. The Parker spiral angle distributions measured at different radial distances from the Sun in the interplanetary magnetic field at Mercury between perihelion and aphelion. Each distribution of Parker spiral angles is normalized between 0 and 1, where the peak of each distribution is in yellow. The solid black line represents the peak of a Gaussian fitted to each distribution. The dotted line shows the angle predicted by *Coleman* [1966].

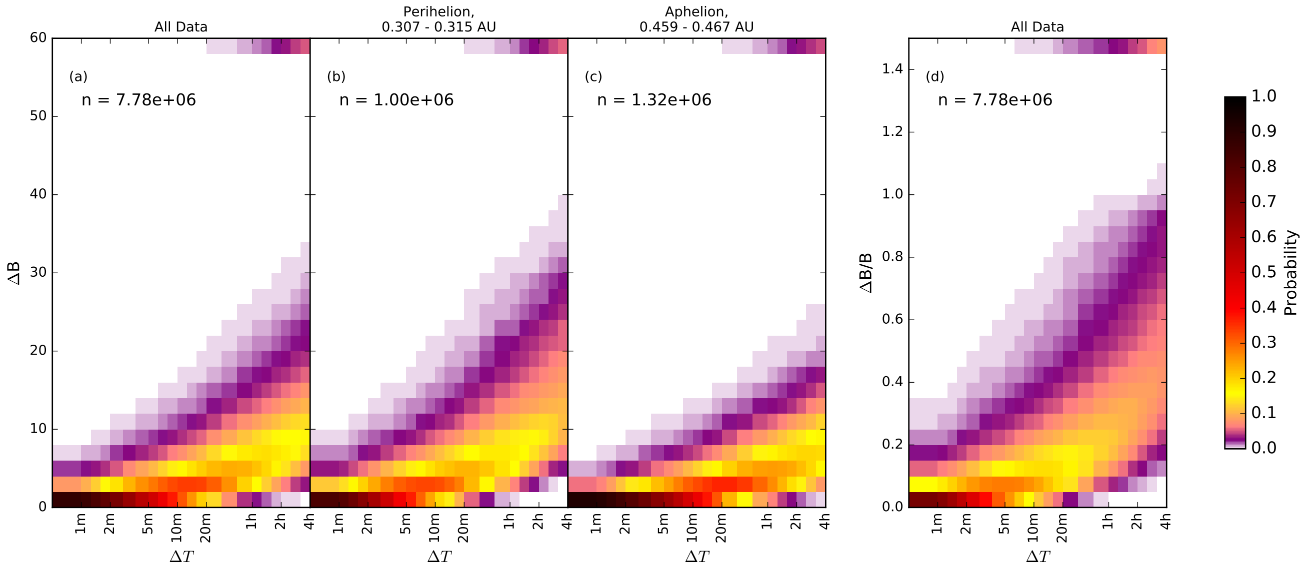

Figure 5. Probabilities of a change in magnetic field magnitude with time for a) all data, b) data from near Mercury's orbital perihelion and c) near Mercury's aphelion. The x-axis of each panel is a logarithmic scale of time, while the y-axis shows the change in field magnitude. The color of each grid cell represents a probability between 0 and 1, and is presented using a logarithmic scale to emphasize the probability distributions. Panel d) is similar to panel a, but the change in magnetic field strength has been scaled by the initial measured field strength.

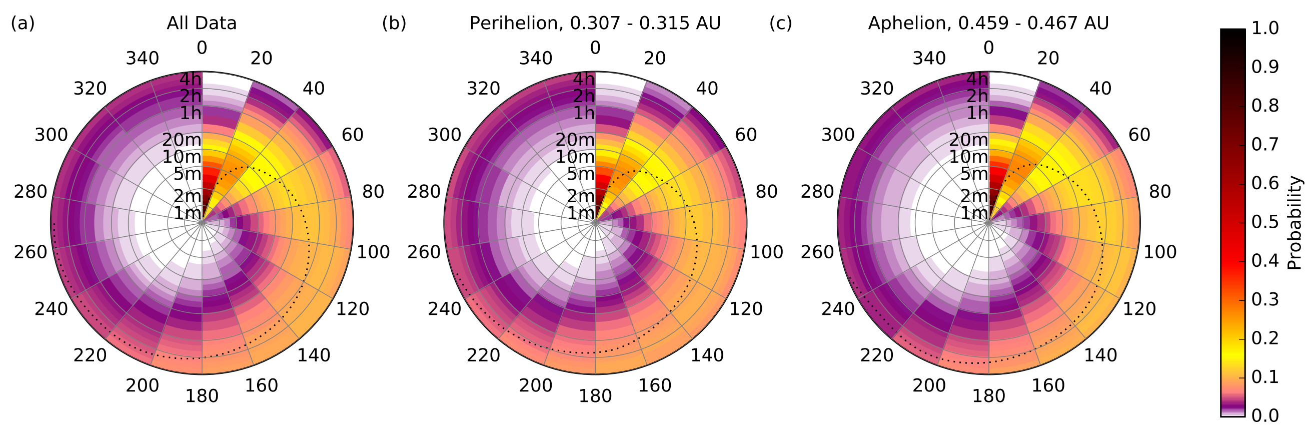

Figure 6. Probability of a change in clock angle (circular axis) as a function of time (radial axis). Panel a) shows the probability for all IMF data, b) shows the probability near perihelion and c) near aphelion. The same logarithmic color scale is used as in Figure 5 and a dotted line shows how the peak of the distribution varies with time.

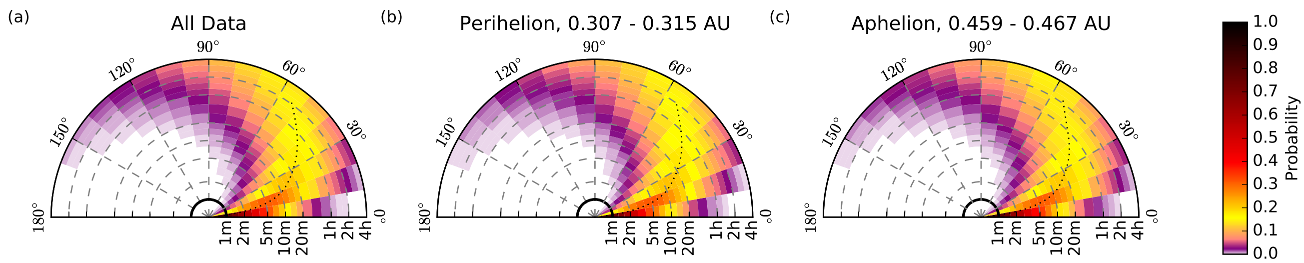

Figure 7. Panels a), b) and c) show the probability of a change in cone angle (circular axis) with time (radial axis) for all IMF data, near perihelion and near aphelion, respectively. As in Figure 6, the dashed line shows the peak of the probability distribution with time.

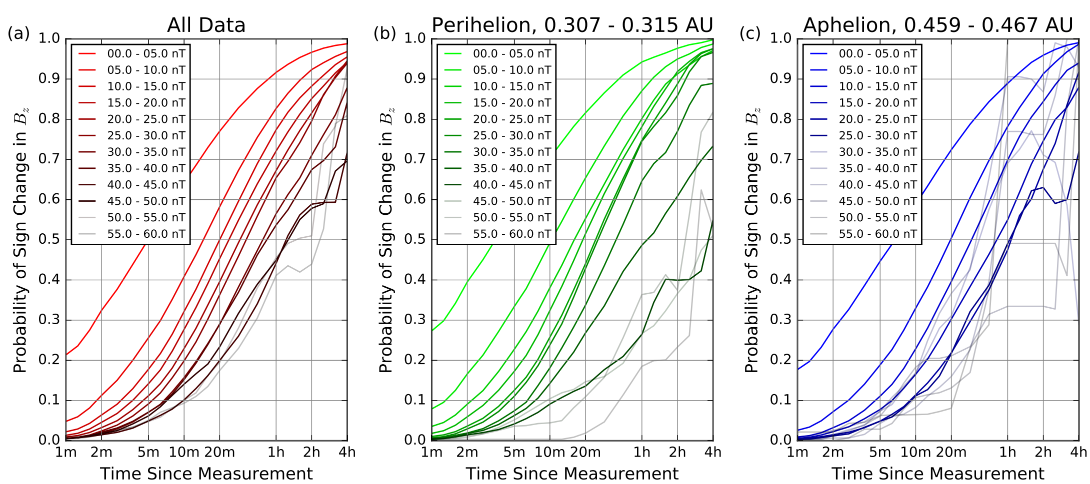

Figure 8. Probabilities of a change in polarity of the z component of the IMF for: (a) all data; (b) near perihelion; (c) near aphelion as a function of time. Each different line represents the probability of a sign change occurring for an initial IMF magnitude within one of the 5 nT bins listed in the legend of each panel. Some lines with higher starting IMF magnitudes are grayed out in each plot as there are not enough instances of such field strengths to create a reliable probability function.

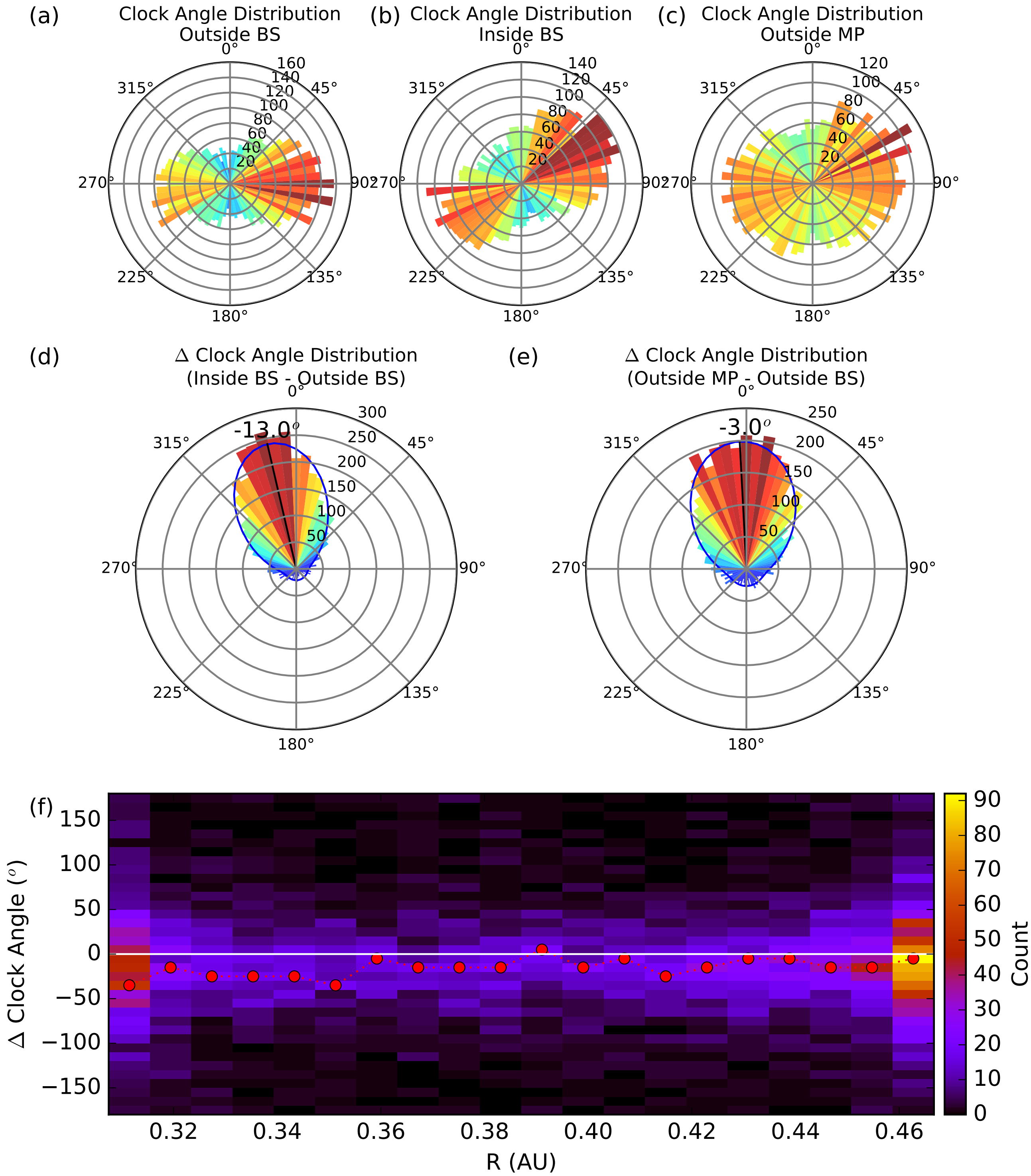

Figure 9. Panels a), b) and c) show a 10 minute average of a subset of clock angles collected just outside of the bow shock (IMF), just within the bow shock (magnetosheath) and just outside the magnetopause (magnetosheath), respectively, using the same format as the clock angle plots in Figure 1. Panels d) and e) show the distributions of the difference in clock angle between the magnetosheath and the interplanetary magnetic field near the bow shock d) and near the magnetopause e). Panel f shows how the change in clock angle between the interplanetary magnetic field and the magnetosheath varies

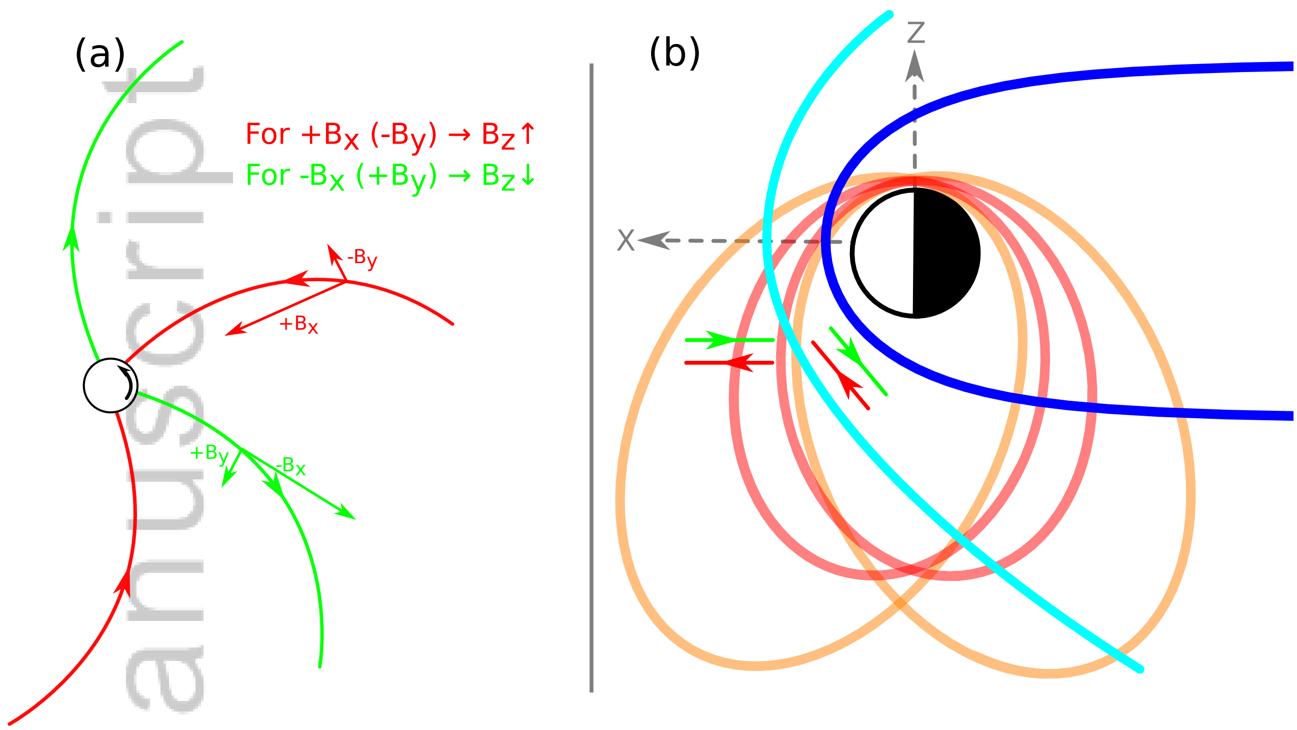

Figure 10. A schematic to explain the rotation of the clock angle distributions observed in Figure 1. Panel a is in the stationary frame looking down on the northern hemisphere of the Sun, where sunward (red) and antisunward (green) field lines form an Archimedian spiral due to the rotation of the Sun as described by [*Parker*, 1958]. Panel b is in the frame facing the dusk side of Mercury, where the Sun is to the left in the x direction. The magnetopause is represented by the solid dark blue line and the bow shock is in cyan. The 12 and 8 hour orbital configurations of MESSENGER are presented in orange and red, respectively. The sunward and antisunward field lines of a are depicted to be mostly radial ($B_{IMF} \sim \pm B_x$) upstream of the bow shock. Downstream of the shock, these field lines have obtained a component in the $\pm z$ direction as they are shocked and draped around the magnetopause.

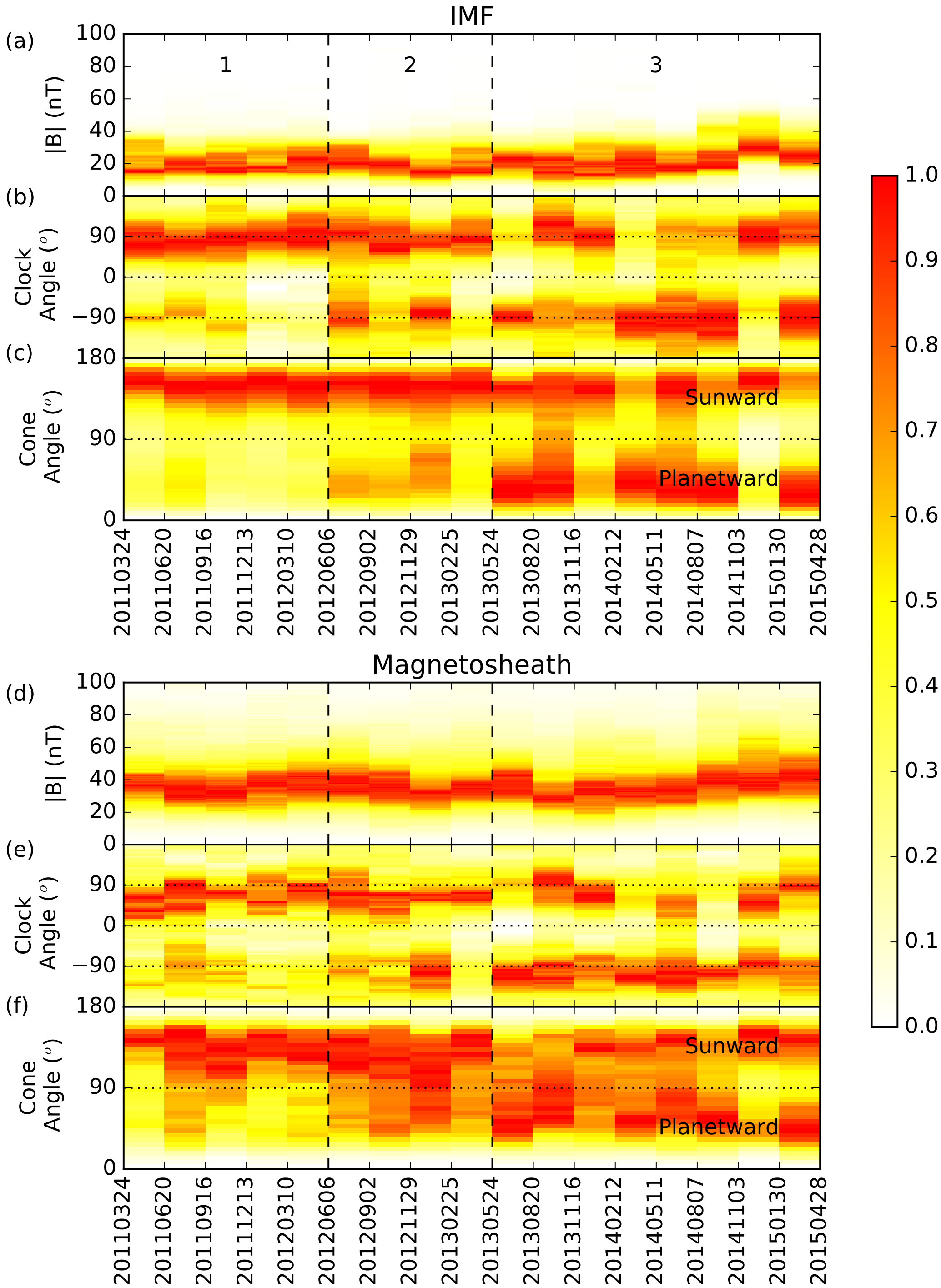

Figure 11. A time series of field magnitude (a and d), clock angle (b and e) and cone angle(c and f) distributions spanning approximately the entire orbital phase of the MESSENGER mission. Panels a - c show the parameter distributions detected in the interplanetary magnetic field data and panels d - f are magnetosheath distributions. Each time series bin is one Mercury year (~88 Earth days) in duration to remove any orbital effects. Each distribution is normalized to lie between 0 and 1, where white represents a low count and red represents a high count. Vertical dashed lines separate the plots into three different time periods.

Figure 1.

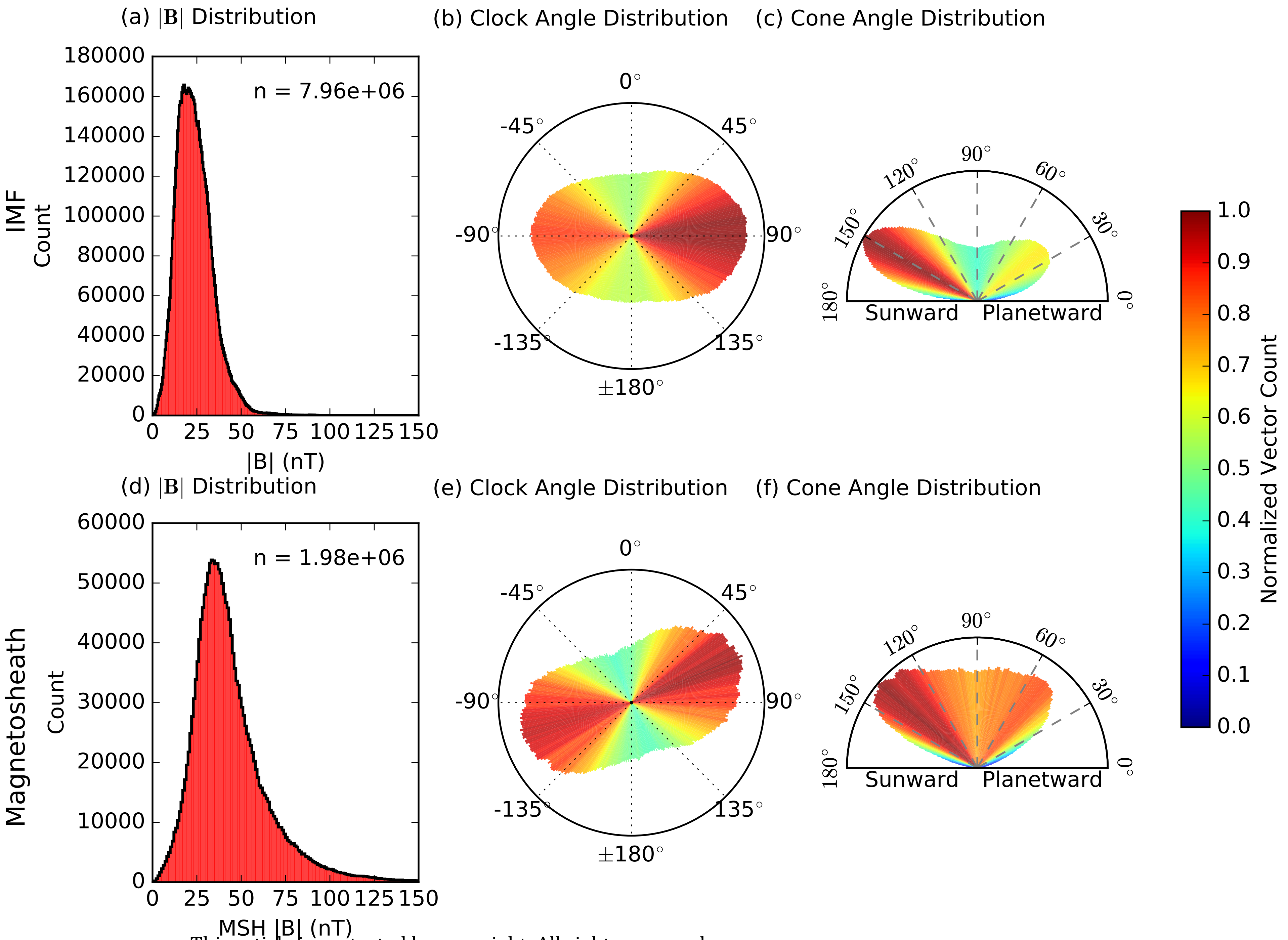
(a) |B| Distribution
(b) Clock Angle Distribution
(c) Cone Angle Distribution
IMF
Count
n = 7.96e+06
180000
160000
140000
120000
100000
80000
60000
40000
20000
0
0 25 50 75 100 125 150
|B| (nT)
0°
45°
90°
135°
±180°
-135°
-90°
-45°
90°
60°
30°
0°
120°
150°
180°
Sunward
Planetward
(d) |B| Distribution
(e) Clock Angle Distribution
(f) Cone Angle Distribution
Magnetosheath
Count
n = 1.98e+06
60000
50000
40000
30000
20000
10000
0
0 25 50 75 100 125 150
MSH |B| (nT)
Normalized Vector Count
1.0
0.9
0.8
0.7
0.6
0.5
0.4
0.3
0.2
0.1
0.0

Figure 2.

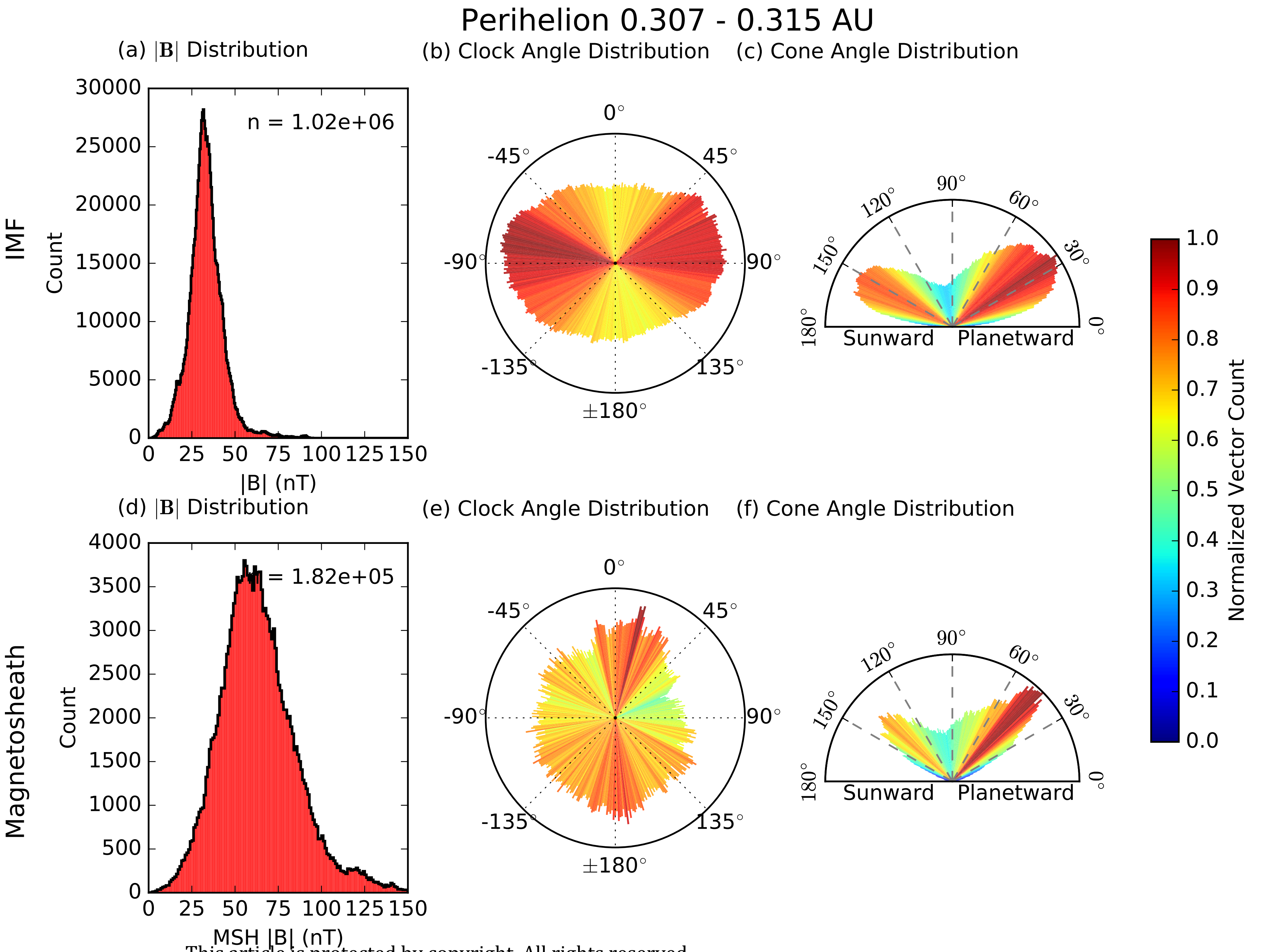
Perihelion 0.307 - 0.315 AU
(a) |B| Distribution
(b) Clock Angle Distribution
(c) Cone Angle Distribution
IMF
Count
n = 1.02e+06
|B| (nT)
0°
45°
90°
135°
±180°
-135°
-90°
-45°
90°
120°
60°
150°
30°
180°
0°
Sunward
Planetward
(d) |B| Distribution
(e) Clock Angle Distribution
(f) Cone Angle Distribution
Magnetosheath
= 1.82e+05
MSH |B| (nT)
Normalized Vector Count

Figure 3.

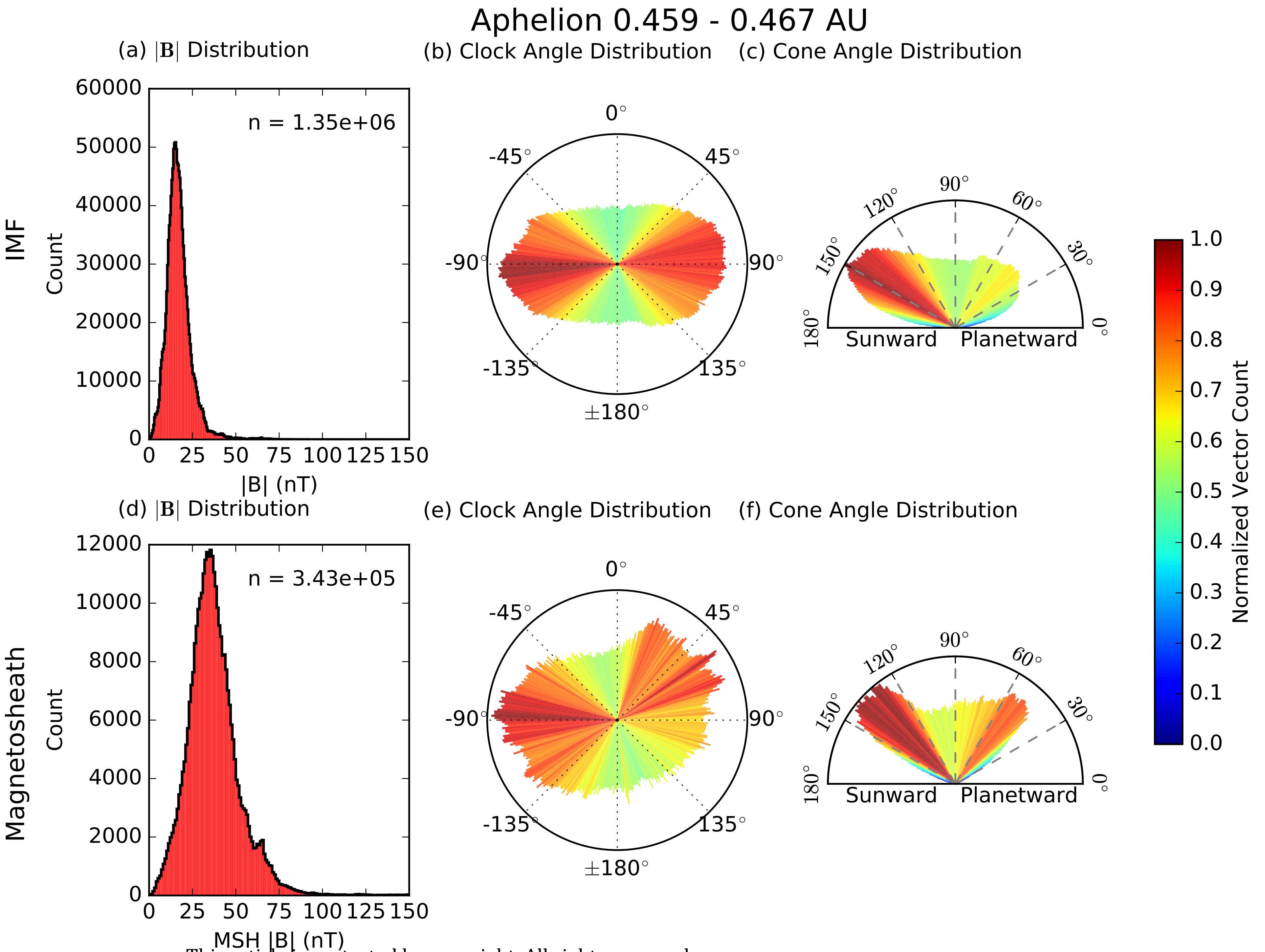

Aphelion 0.459 - 0.467 AU
(a) |B| Distribution
(b) Clock Angle Distribution
(c) Cone Angle Distribution
IMF
Count
n = 1.35e+06
|B| (nT)
0°
45°
90°
135°
±180°
-135°
-90°
-45°
90°
60°
30°
0°
120°
150°
180°
Sunward
Planetward
(d) |B| Distribution
(e) Clock Angle Distribution
(f) Cone Angle Distribution
Magnetosheath
Count
n = 3.43e+05
MSH |B| (nT)
Normalized Vector Count

Figure 4.

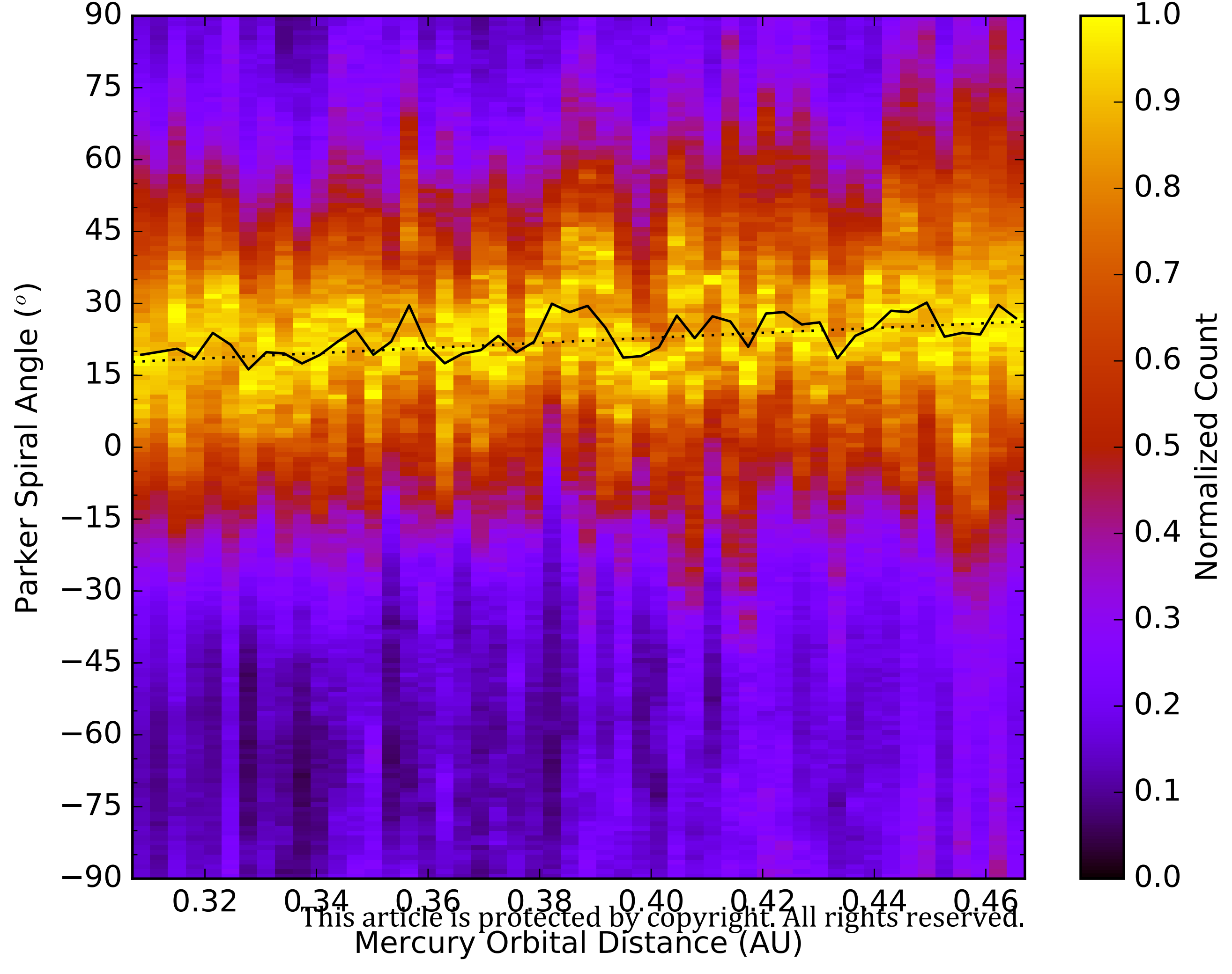

Parker Spiral Angle (°)
Mercury Orbital Distance (AU)
Normalized Count
90
75
60
45
30
15
0
−15
−30
−45
−60
−75
−90
0.32
0.34
0.36
0.38
0.40
0.42
0.44
0.46
1.0
0.9
0.8
0.7
0.6
0.5
0.4
0.3
0.2
0.1
0.0

Figure 5.

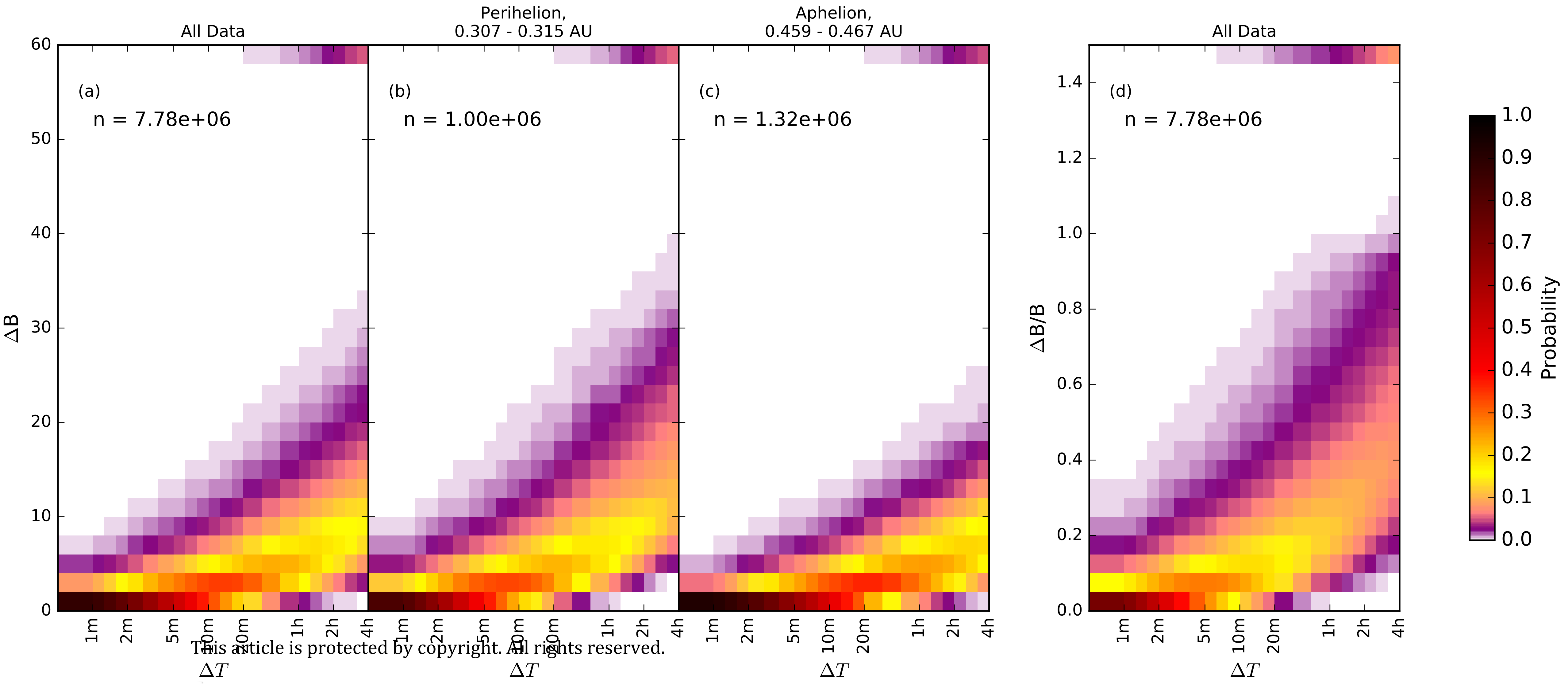
All Data
Perihelion,
0.307 - 0.315 AU
Aphelion,
0.459 - 0.467 AU
All Data
(a)
n = 7.78e+06
(b)
n = 1.00e+06
(c)
n = 1.32e+06
(d)
n = 7.78e+06
ΔB
ΔB/B
ΔT
Probability

Figure 6.

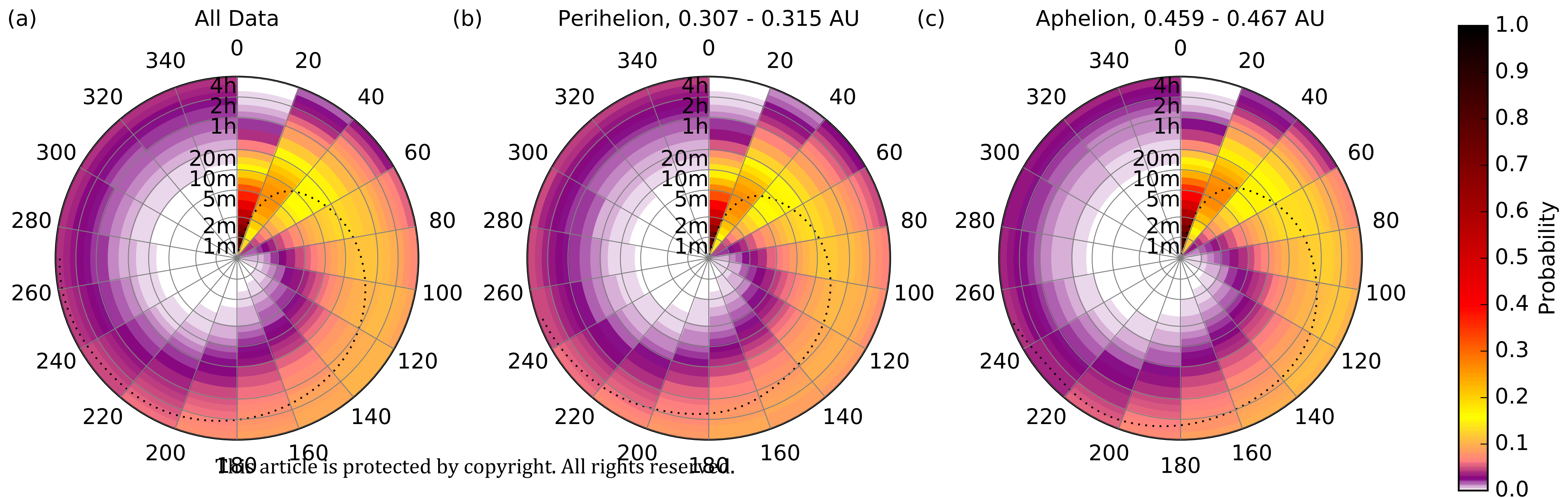

(a)
All Data
(b)
Perihelion, 0.307 - 0.315 AU
(c)
Aphelion, 0.459 - 0.467 AU
0
20
40
60
80
100
120
140
160
180
200
220
240
260
280
300
320
340
4h
2h
1h
20m
10m
5m
2m
1m
Probability
0.0
0.1
0.2
0.3
0.4
0.5
0.6
0.7
0.8
0.9
1.0

Figure 7.

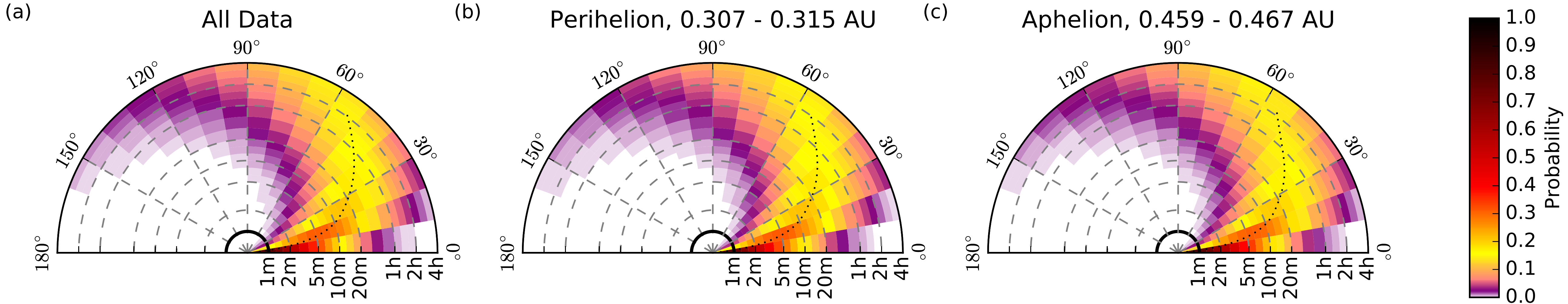
(a)
All Data
(b)
Perihelion, 0.307 - 0.315 AU
(c)
Aphelion, 0.459 - 0.467 AU
90°
120°
60°
150°
30°
180°
0°
1m
2m
5m
10m
20m
1h
2h
4h
Probability
1.0
0.9
0.8
0.7
0.6
0.5
0.4
0.3
0.2
0.1
0.0

Figure 8.

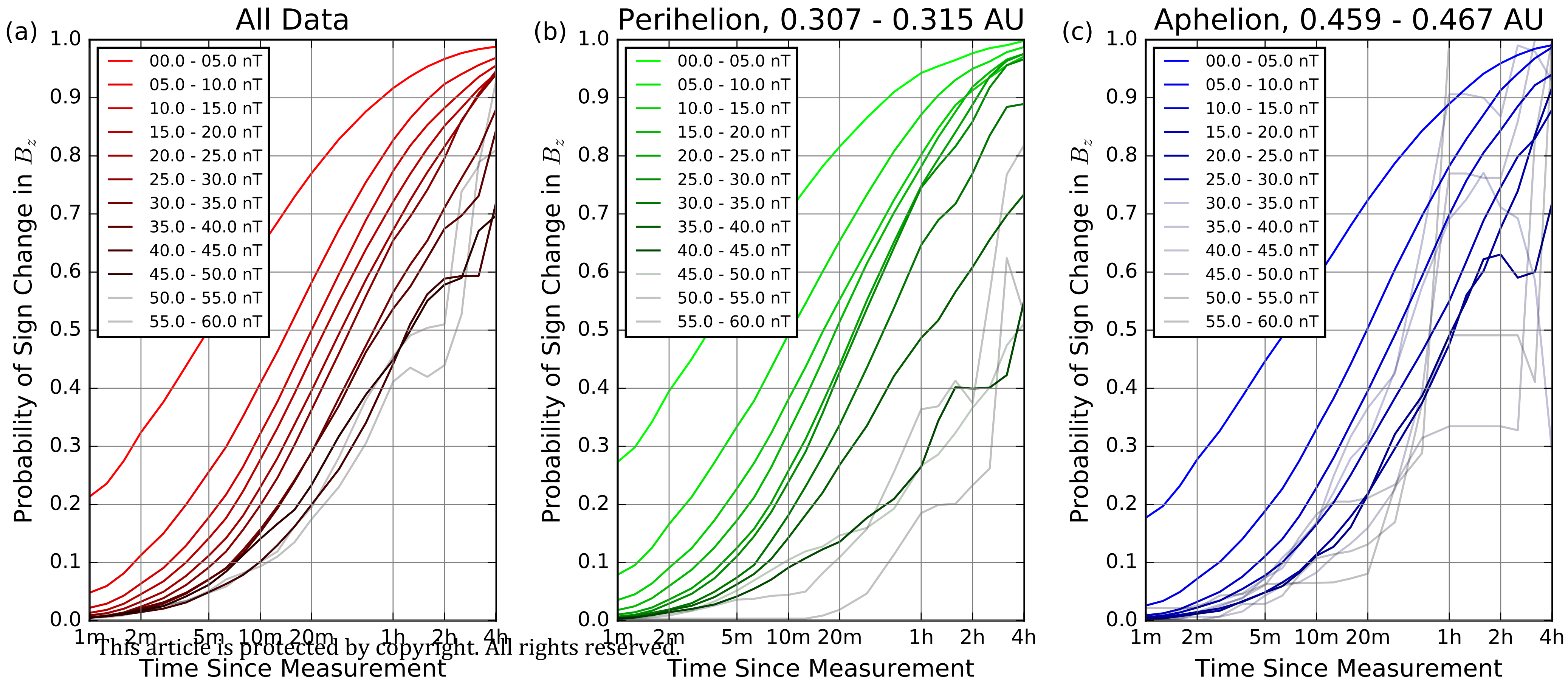

(a)
All Data
(b)
Perihelion, 0.307 - 0.315 AU
(c)
Aphelion, 0.459 - 0.467 AU
Probability of Sign Change in B_z
Time Since Measurement
1m
2m
5m
10m
20m
1h
2h
4h
0.0
0.1
0.2
0.3
0.4
0.5
0.6
0.7
0.8
0.9
1.0
00.0 - 05.0 nT
05.0 - 10.0 nT
10.0 - 15.0 nT
15.0 - 20.0 nT
20.0 - 25.0 nT
25.0 - 30.0 nT
30.0 - 35.0 nT
35.0 - 40.0 nT
40.0 - 45.0 nT
45.0 - 50.0 nT
50.0 - 55.0 nT
55.0 - 60.0 nT

Figure 9.

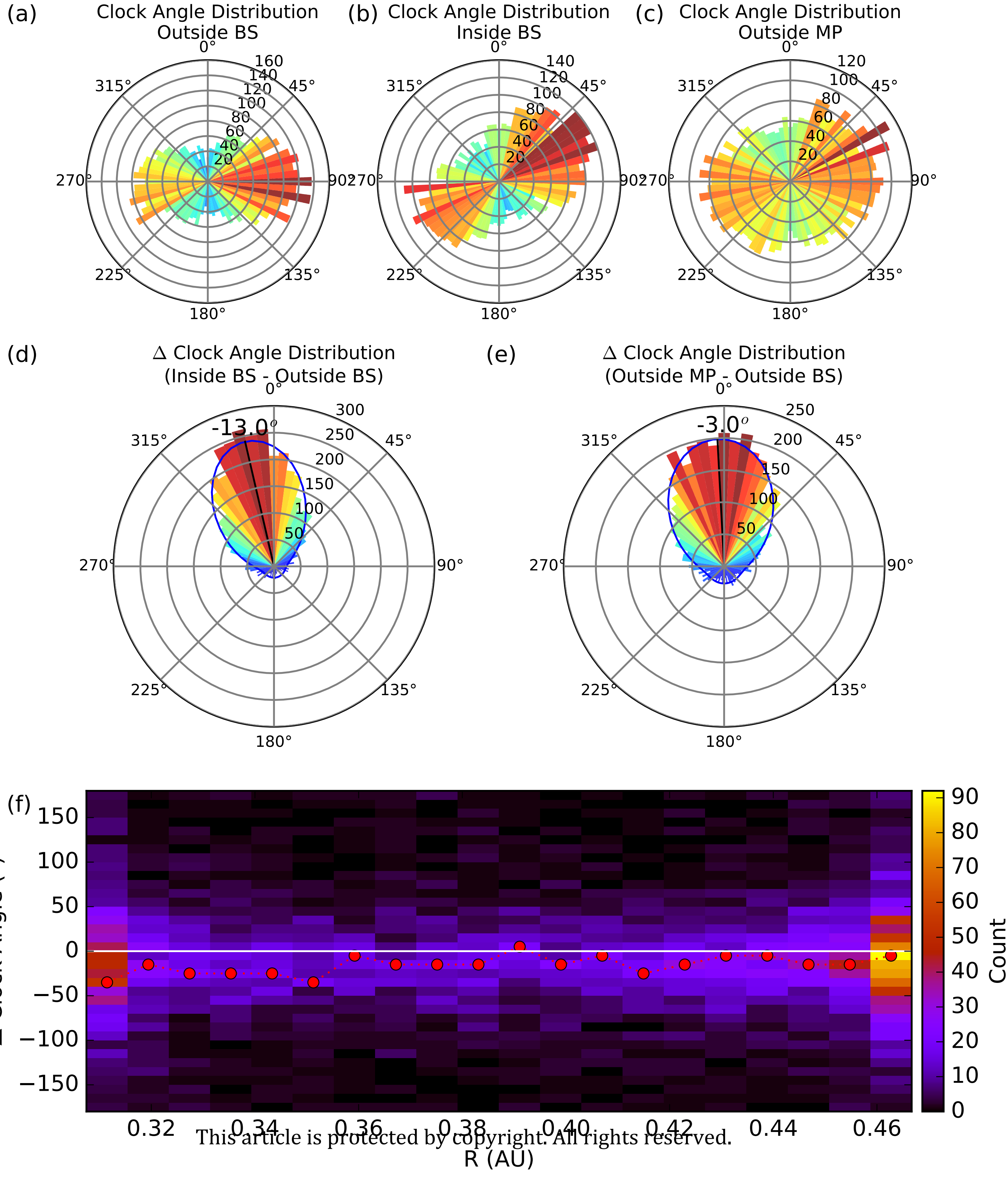
(a)
Clock Angle Distribution
Outside BS
(b)
Clock Angle Distribution
Inside BS
(c)
Clock Angle Distribution
Outside MP
(d)
Δ Clock Angle Distribution
(Inside BS - Outside BS)
-13.0°
(e)
Δ Clock Angle Distribution
(Outside MP - Outside BS)
-3.0°
(f)
Δ Clock Angle (°)
R (AU)
Count

Figure 10.

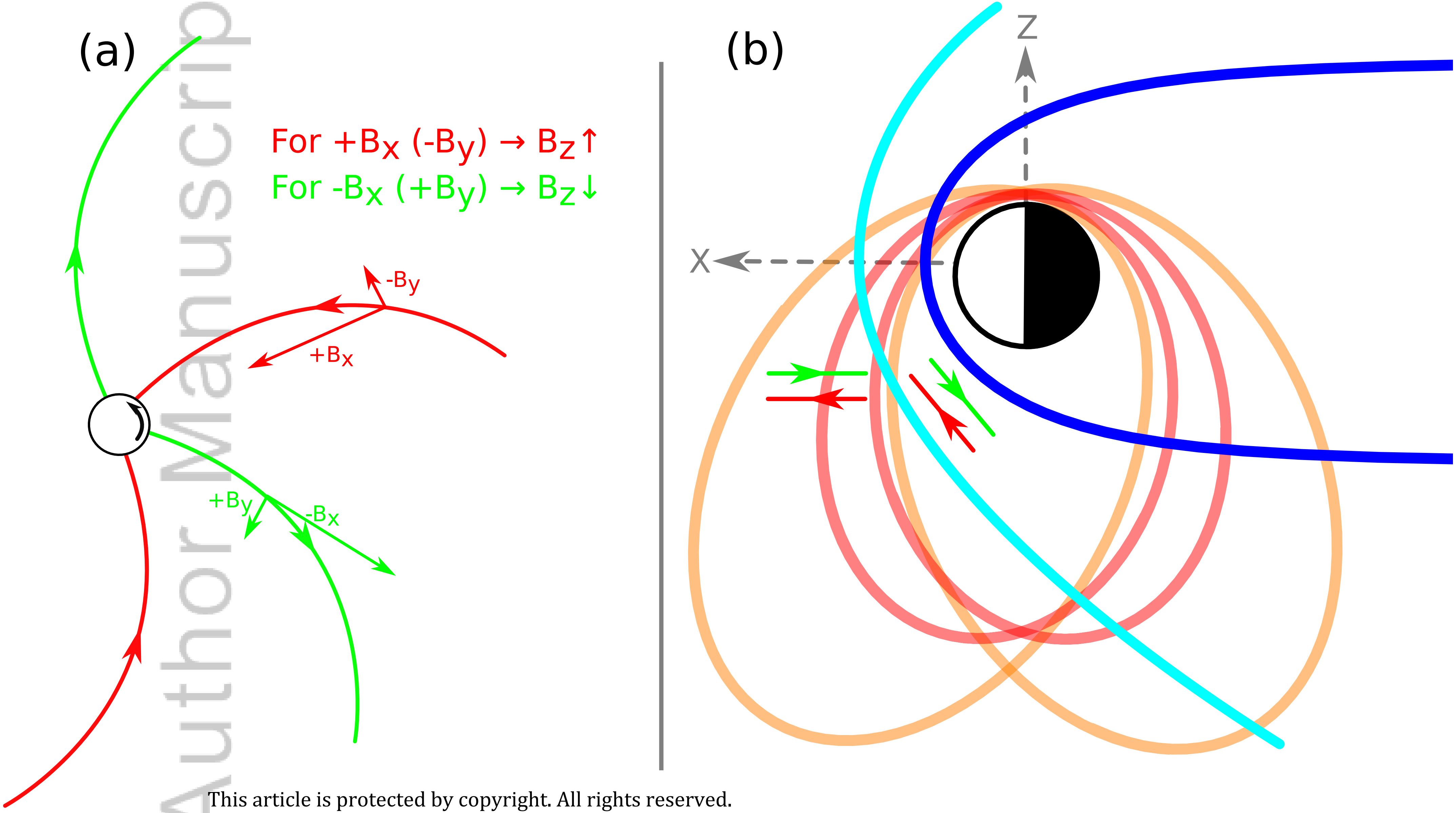
(a)
For +Bx (-By) → Bz↑
For -Bx (+By) → Bz↓
-By
+Bx
+By
-Bx
(b)
Z
X

Figure 11.

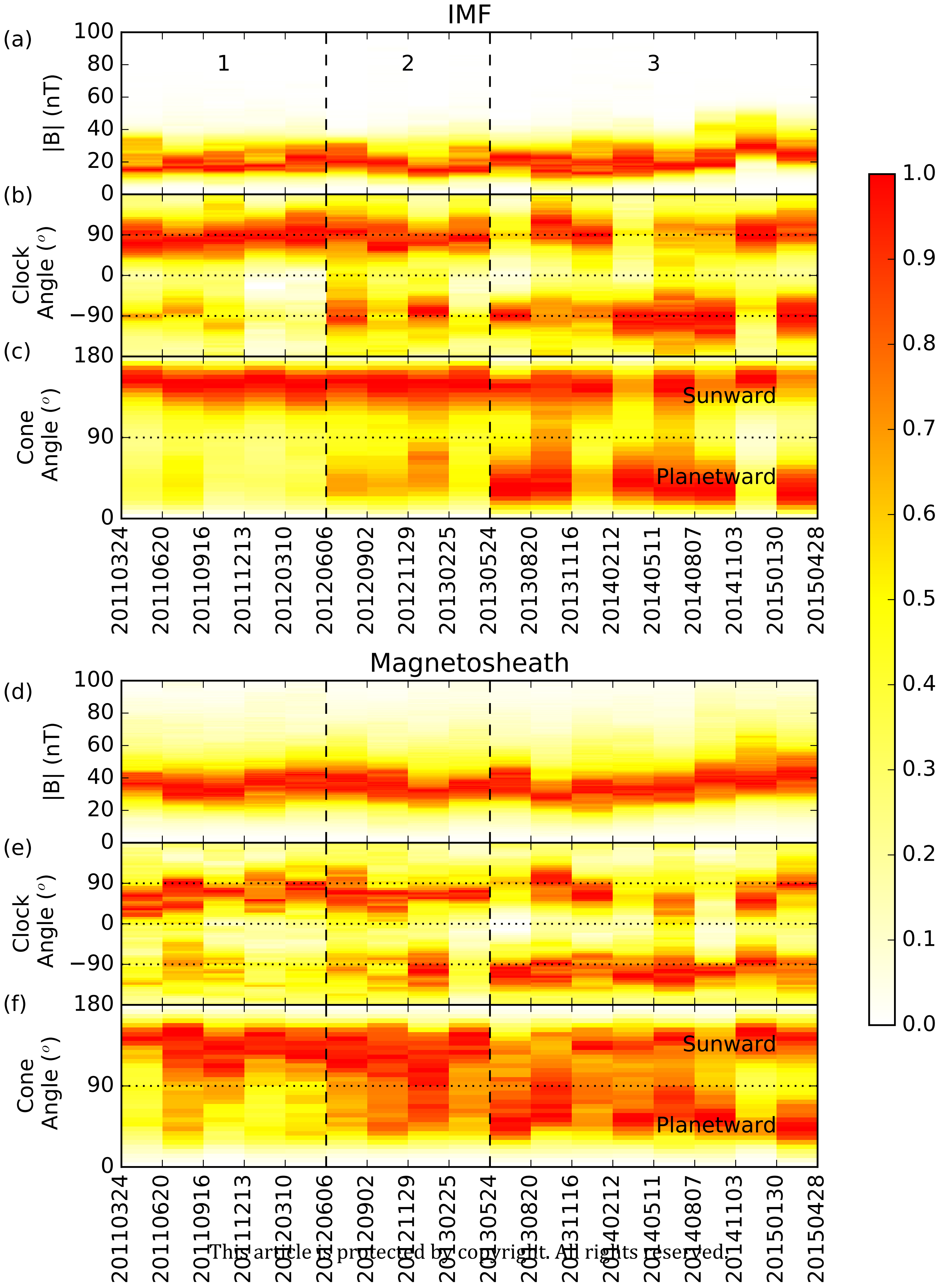
IMF
(a)
(b)
(c)
|B| (nT)
Clock Angle (°)
Cone Angle (°)
1
2
3
Sunward
Planetward
20110324
20110620
20110916
20111213
20120310
20120606
20120902
20121129
20130225
20130524
20130820
20131116
20140212
20140511
20140807
20141103
20150130
20150428
Magnetosheath
(d)
(e)
(f)
1.0
0.9
0.8
0.7
0.6
0.5
0.4
0.3
0.2
0.1
0.0